

Matriptase activation of Gq drives epithelial disruption and inflammation via RSK and DUOX

Jiajia Ma¹, Claire A Scott^{2,3}, Ying Na Ho¹, Harsha Mahabaleshwar¹, Katherine S Marsay^{2,4}, Changqing Zhang¹, Christopher KJ Teow¹, Ser Sue Ng², Weibin Zhang², Vinay Tergaonkar², Lynda J Partridge⁴, Sudipto Roy^{2,5,6}, Enrique Amaya³, Tom J Carney^{1,2*}

¹Lee Kong Chian School of Medicine, Experimental Medicine Building, Yunnan Garden Campus, 59 Nanyang Drive, Nanyang Technological University, Singapore, Singapore; ²Institute of Molecular and Cell Biology (IMCB), A*STAR (Agency for Science, Technology and Research), Singapore, Singapore; ³Division of Cell Matrix Biology and Regenerative Medicine, School of Biological Sciences, Faculty of Biology, Medicine and Health, University of Manchester, Manchester, United Kingdom; ⁴Department of Molecular Biology and Biotechnology, University of Sheffield, Sheffield, United Kingdom; ⁵Department of Biological Sciences, National University of Singapore, Singapore, Singapore; ⁶Department of Pediatrics, Yong Loo Ling School of Medicine, National University of Singapore, Singapore, Singapore

Abstract Epithelial tissues are primed to respond to insults by activating epithelial cell motility and rapid inflammation. Such responses are also elicited upon overexpression of the membrane-bound protease, Matriptase, or mutation of its inhibitor, Hai1. Unrestricted Matriptase activity also predisposes to carcinoma. How Matriptase leads to these cellular outcomes is unknown. We demonstrate that zebrafish *hai1a* mutants show increased H₂O₂, NfκB signalling, and IP₃R-mediated calcium flashes, and that these promote inflammation, but do not generate epithelial cell motility. In contrast, inhibition of the Gq subunit in *hai1a* mutants rescues both the inflammation and epithelial phenotypes, with the latter recapitulated by the DAG analogue, PMA. We demonstrate that *hai1a* has elevated MAPK pathway activity, inhibition of which rescues the epidermal defects. Finally, we identify RSK kinases as MAPK targets disrupting adherens junctions in *hai1a* mutants. Our work maps novel signalling cascades mediating the potent effects of Matriptase on epithelia, with implications for tissue damage response and carcinoma progression.

*For correspondence: tcarney@ntu.edu.sg

Competing interests: The authors declare that no competing interests exist.

Funding: See page 27

Received: 15 January 2021

Accepted: 23 June 2021

Published: 24 June 2021

Reviewing editor: Jonathan A Cooper, Fred Hutchinson Cancer Research Center, United States

© Copyright Ma et al. This article is distributed under the terms of the [Creative Commons Attribution License](#), which permits unrestricted use and redistribution provided that the original author and source are credited.

Introduction

The transmembrane serine protease, Matriptase, encoded by the *ST14* gene, has potent oncogenic properties and is consistently dysregulated in human carcinomas. Overexpression of Matriptase in the mouse epidermis leads to epidermal papillomas, ulcerative and invasive carcinomas, and inflammation (*List et al., 2005; Martin and List, 2019*). These effects of Matriptase are mitigated by a cognate serine protease inhibitor, HAI-1. Clinically, an increase in the Matriptase:HAI-1 ratio has been found in a range of tumours and is predictive of poor outcome (*Martin and List, 2019*). Loss of mouse Hai1 leads to epidermal and intestinal barrier defects, epithelial inflammation, and failure of placental labyrinth formation, which are all due to unrestricted Matriptase activity (*Kawaguchi et al., 2011; Nagaike et al., 2008; Szabo et al., 2007*). The response of epithelia to

eLife digest Cancer occurs when normal processes in the cell become corrupted or unregulated. Many proteins can contribute, including one enzyme called Matriptase that cuts other proteins at specific sites. Matriptase activity is tightly controlled by a protein called Hai1. In mice and zebrafish, when Hai1 cannot adequately control Matriptase activity, invasive cancers with severe inflammation develop. However, it is unclear how unregulated Matriptase leads to both inflammation and cancer invasion.

One outcome of Matriptase activity is removal of proteins called Cadherins from the cell surface. These proteins have a role in cell adhesion: they act like glue to stick cells together. Without them, cells can dissociate from a tissue and move away, a critical step in cancer cells invading other organs. However, it is unknown exactly how Matriptase triggers the removal of Cadherins from the cell surface to promote invasion.

Previous work has shown that Matriptase switches on a receptor called Proteinase-activated receptor 2, or Par2 for short, which is known to activate many enzymes, including one called phospholipase C. When activated, this enzyme releases two signals into the cell: a sugar called inositol triphosphate, IP3; and a lipid or fat called diacylglycerol, DAG. It is possible that these two signals have a role to play in how Matriptase removes Cadherins from the cell surface.

To find out, Ma et al. mapped the effects of Matriptase in zebrafish lacking the Hai1 protein. This revealed that Matriptase increases IP3 and DAG levels, which initiate both inflammation and invasion. IP3 promotes inflammation by switching on pro-inflammatory signals inside the cell such as the chemical hydrogen peroxide. At the same time, DAG promotes cell invasion by activating a well-known cancer signalling pathway called MAPK. This pathway activates a protein called RSK. Ma et al. show that this protein is required to remove Cadherins from the surface of cells, thus connecting Matriptase's activation of phospholipase C with its role in disrupting cell adhesion.

An increase in the ratio of Matriptase to HAI-1 (the human equivalent of Hai1) is present in many cancers. For this reason, the signal cascades described by Ma et al. may be of interest in developing treatments for these cancers. Understanding how these signals work together could lead to more direct targeted anti-cancer approaches in the future.

unregulated Matriptase activity appears conserved across vertebrates. Mutation of the zebrafish orthologue, Hai1a, also results in epidermal defects, including loss of membrane E-cadherin, aberrant mesenchymal behaviour of keratinocytes, which form cell aggregations over the body and loss of fin fold integrity. The epidermis also displays sterile inflammation and is invaded by highly active neutrophils. Genetic ablation of the myeloid lineage demonstrated that the keratinocyte phenotypes are not a consequence of the inflammation (Carney et al., 2007). The strong *hai1a^{fr26}* allele is embryonic lethal, dying within the first week, whilst the more mild allele, *hai1a^{hi2217}*, is semi-viable, with epithelial defects resolved through sphingosine-1-phosphate-mediated entosis and cell extrusion (Armistead et al., 2020). All *hai1a* mutant phenotypes can be ameliorated by reduction of Matriptase levels (Carney et al., 2007; Mathias et al., 2007).

Due to the clinical implications of its dysregulation, the signalling pathways activated pathologically by Matriptase are of interest. The G-protein-coupled receptor, proteinase-activated receptor-2 (Par2), is essential for the oncogenic and inflammatory effects of uninhibited Matriptase in zebrafish and mouse (Sales et al., 2015; Schepis et al., 2018). Par2 is directly activated by Matriptase proteolysis and signals through a number of heterotrimeric G α protein subunits. Early studies in keratinocytes linked Par2 activation with intracellular Ca⁺⁺ mobilisation via phospholipase C, thus implicating Gq subunit as the canonical target (Schechter et al., 1998). Alternate G α subunits, including Gi, Gs, and G12/13, are now known to also be activated by Par2 (Zhao et al., 2014). Par2 displays biased agonism, and the logic of the pathway utilised depends on cell context and the activating protease. In vitro experiments using HEK293 cells implicated both Par2 and Gi in Matriptase-mediated Nf κ b pathway activation (Sales et al., 2015). Whilst this explains the inflammatory phenotype of uninhibited Matriptase, it does not address whether Par2 promotes carcinoma phenotypes directly in keratinocytes in vivo. In zebrafish, as the keratinocyte defects are not dependent on inflammation, but are dependent on Par2, it is likely that there is a direct effect of Par2 on promoting keratinocyte motility.

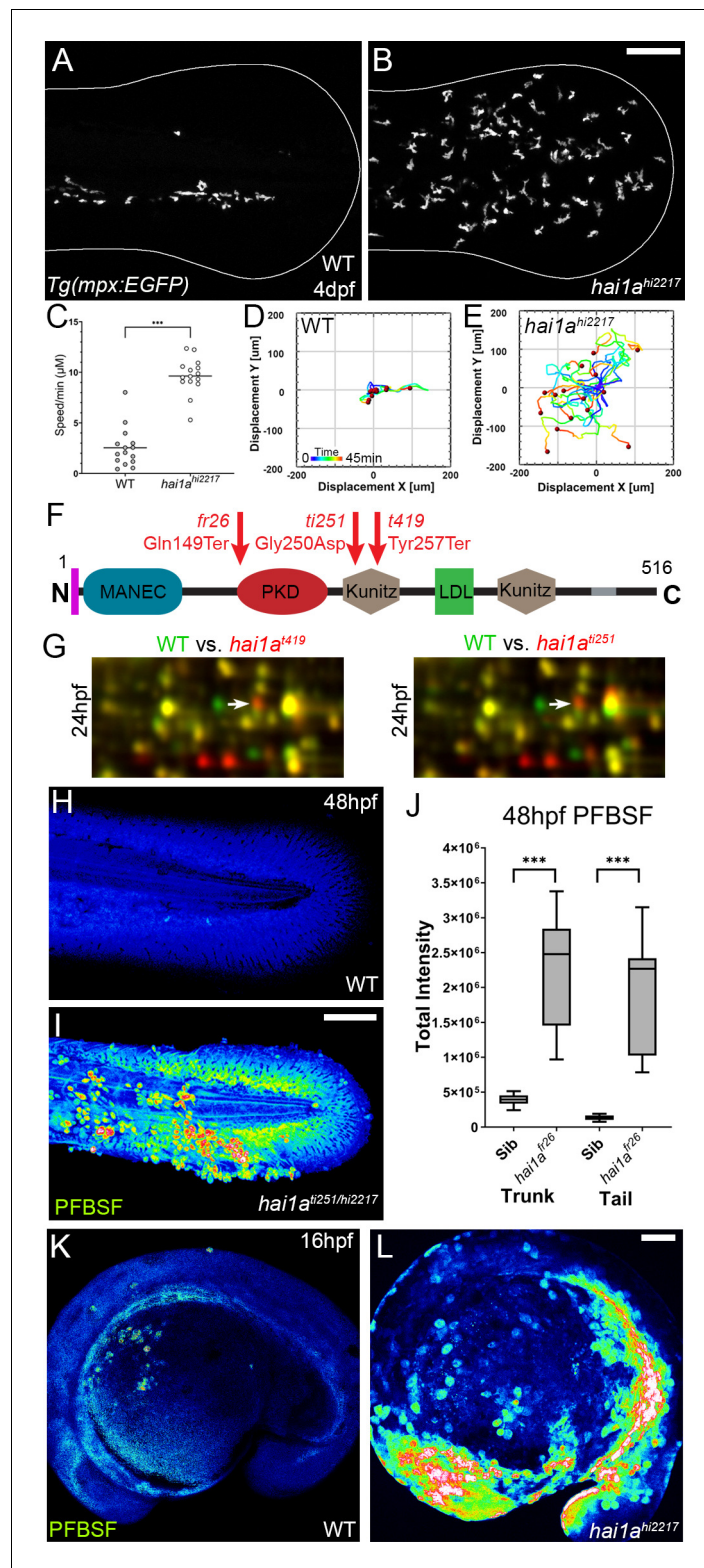


Figure 1. The epidermis of *hai1a* mutants displays elevated hydrogen peroxide. (A, B) Projected confocal images showing neutrophils populate the tail of *hai1a^{hi2217}* mutants (B) but just the vasculature of WT (A) at 4dpf labelled by the *Tg(mpx:EGFP)¹¹⁴* line. Fin extremity outlined in white. (C) Neutrophils move significantly faster in *hai1a^{hi2217}* than WT. n = 15; t-test; ***p<0.001. (D, E) Tracks of neutrophil migration taken from **Video 1** in WT (D) and *hai1a^{hi2217}* (E). (F) Schematic of the Hai1a protein with protein domains given, signal peptide as purple line and **Figure 1 continued on next page**

Figure 1 continued

transmembrane domain as grey line. Location and nature of the *fr26* and two *dandruff* alleles, *ti251* and *t419* given. (G) Selected region of 2D gel of protein extracted from 24hpf embryos for *hai1a*^{t419} (left) or *hai1a*^{ti251} (right) in red, superimposed over WT protein samples (green in both). The shift in pI of peroxiredoxin4 in both alleles is indicated with an arrow. (H, I) Projected lateral confocal views of pentafluorobenzene sulfonyl fluorescein (PFBSF) staining of WT (H) and *hai1a*^{ti251/hi2217} (I) tail fins at 48hpf. (J) Box and whiskers plot of PFBSF fluorescent staining intensity of WT and *hai1a*^{fr26} mutants at 48hpf in trunk and tail. n = 9; t-test ***p < 0.001. (K, L) Projected lateral confocal views of PFBSF staining of WT (K) and *hai1a*^{hi2217} (L) at 16hpf. Scale bars: (B, I, L) = 100 μm.

The online version of this article includes the following source data and figure supplement(s) for figure 1:

Source data 1. 2D proteomics protein ID report list of the spot identities with significant ratio changes.

Source data 2. 2D proteomics protein ratio changes for each of the protein spots identified as significantly changed.

Source data 3. 2D proteomics top 50 proteins significantly changed in *hai1a* mutants.

Figure supplement 1. The epidermis of *hai1a* mutants displays elevated hydrogen peroxide.

Par2 can also transactivate EGFR through an unknown mechanism, and inhibition of EGFR alleviates certain basal keratinocyte phenotypes of zebrafish *hai1a* mutants (Schepis et al., 2018). Thus, the identity, contribution, and interactions of the pathways downstream of Matriptase and Par2 remain unclear. Here through use of the zebrafish *hai1a* mutant, we comprehensively map the essential pathways downstream of zebrafish Matriptase and Par2, leading to inflammation and epithelial disruption.

Results

Increased hydrogen peroxide and calcium flashes contribute to inflammation in *hai1a* mutants

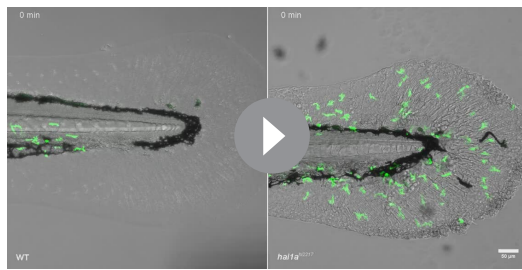
Neutrophils in *hai1a* embryos invade the epidermis, are highly motile, but move randomly (Carney et al., 2007; Mathias et al., 2007; Figure 1A–E, Video 1). To establish the nature of their stimulus, we tested if neutrophils in *hai1a* altered their behaviour in the presence of a large fin wound. In wild-type larvae, neutrophils were recruited from a great distance and tracked to the wound with high directionality. However, neutrophils in the *hai1a* mutant appeared largely apathetic to the wound and remained migrating randomly. There was a mild increase in neutrophil speed in *hai1a* larvae following wounding, indicating that they retain capacity to respond to additive stimuli (Figure 1—figure supplement 1A–D, Video 2). Co-labelling of basal keratinocyte nuclei (using TP63 immunostaining), neutrophils (*Tg(fli1:EGFP)*¹ transgenic), and TUNEL labelling of apoptotic cells highlighted that whilst the epidermis of *hai1a* mutants, unlike WT, had regions of apoptosis at 24hpf (arrowhead, Figure 1—figure supplement 1E, F), neutrophils were not associated, but rather found at nascent TUNEL-negative aggregates of basal keratinocytes (arrow). We conclude that epidermal cell death does not directly contribute to inflammation and that the effector stimulating neutrophils in *hai1a* mutants is as, or more, potent as that of wounds.

To identify the neutrophil activator in *hai1a*, we employed an unbiased approach using 2D gel proteomics to compare the wild-type proteome with that of strong *hai1a* alleles. The *dandruff* (*ddf*) mutant has many phenotypic similarities to the strong *hai1a*^{fr26} allele (van Eeden et al., 1996). Crosses between *ddf*^{ti251} or *ddf*^{t419} and *hai1a*^{hi2217} failed to complement, and sequencing of *hai1a* cDNA from both *ddf* alleles identified a nonsense mutation in the *ddf*^{t419} allele (c.771T>G; p.Tyr257Ter) and a missense mutation of a highly conserved amino acid in the *ddf*^{ti251} allele (c.749G>A; p.Gly250Asp) (Figure 1F,



Video 1. Neutrophils in WT and *hai1a*^{hi2217} 4dpf larva. Projected confocal timelapses of eGFP-positive neutrophils in the tail region of 4dpf *Tg(mpx:eGFP)*¹¹⁴ (left) and *hai1a*^{hi2217}; *Tg(mpx:eGFP)*¹¹⁴ (right) larvae taken every 45 s for 45 min. Scale bar: 50 μm.

<https://elifesciences.org/articles/66596#video1>



Video 2. Neutrophils in WT and *hai1a*^{hi2217} 4dpf larva before and after fin wound. Projected confocal timelapses of eGFP-positive neutrophils in the tail region of 4dpf *Tg(mpx:eGFP)*ⁱ¹¹⁴ (left) and *hai1a*^{hi2217}; *Tg(mpx:eGFP)*ⁱ¹¹⁴ (right) larvae taken every 50 s for 250 min with the tail fin cut at 50 min. GFP is overlaid on DIC (Differential Interference Contrast) channel. Scale bar: 50 μ m.

<https://elifesciences.org/articles/66596#video2>

Figure 1—figure supplement 1G–I). We used both alleles for comparative 2D protein gel analysis at 24hpf and 48hpf. Rather than finding proteins with altered molecular weight, Peroxiredoxin4 (Prdx4) was identified as having a higher pI in both *hai1a*^{t419} and *hai1a*^{ti251} mutants at 24hpf and 48hpf, indicative of a change in oxidation state (**Figure 1G, Figure 1—figure supplement 1J, K**). Peroxiredoxins are hydrogen peroxide scavengers, and its altered oxidation state suggested that *hai1a* has higher H₂O₂ levels, a known activator of inflammation in larval zebrafish (**Niethammer et al., 2009**). Pentafluorobenzenesulfonyl fluorescein (PFBSF) staining **Maeda et al., 2004** demonstrated significantly higher levels of H₂O₂ in the trunk and tails of *hai1a* mutants at 24hpf and 48hpf (**Figure 1H–J, Figure 1—figure supplement 1L, M**). This increase in H₂O₂ in *hai1a* was observed as early as 16hpf, and thus preceded presentation of *hai1a* phenotypes (**Figure 1K, L**).

To demonstrate that, as with other phenotypes, the H₂O₂ increase in *hai1a* was due to unrestrained activity of Matriptase1a, we used a *matriptase1a* mutant allele, *st14a*^{sq10}, which prematurely terminates the protein at 156 amino acids (**Figure 2A, Figure 2—figure supplement 1A–C; Lin et al., 2019**). Zygotic *st14a* mutants showed no overt phenotype; however, maternal zygotic mutants lacked ear otoliths (**Figure 2B, C**). As expected, when crossed into the *hai1a* background, embryos lacking otoliths (*st14a*^{sq10}; *hai1a*^{hi2217} double mutants) never displayed the *hai1a* epidermal and neutrophil phenotypes (**Figure 2D–F; Table 1**). Double mutants also had significantly reduced H₂O₂ levels (**Figure 2F, Figure 2—figure supplement 1D**). To determine if reduced H₂O₂ could account for the rescue of *hai1a* phenotypes by *st14a* mutation, we used genetic and pharmacological inhibition of the main enzyme responsible for generating H₂O₂ in zebrafish, Duox. A morpholino directed against *duox* successfully reduced H₂O₂ levels (**Figure 2, Figure 2—figure supplement 1D**) and neutrophil inflammation in *hai1a* mutants but did not rescue the epithelial defects (**Figure 2F, G**). Treatment with a known Duox inhibitor, diphenyleneiodonium (DPI), also resulted in amelioration of neutrophil inflammation, but not epithelial aggregates, in *hai1a* mutants (**Figure 2G, Figure 2—figure supplement 1E**). We conclude that Matriptase1 activity leads to excess H₂O₂ in *hai1a* mutants, which partially accounts for the neutrophil inflammation, but not epidermal defects.

Duox is regulated by calcium through its EF-Hand domains, and calcium flashes are known to generate H₂O₂ in epidermal wounds in *Drosophila* (**Razzell et al., 2013**). We injected *hai1a*^{fr26} with RNA encoding the calcium reporter *GCaMP6s*. Timelapse imaging at 24hpf indicated that *hai1a* mutants had significantly more calcium flashes in both the trunk and tail (**Figure 3A, B, E, Figure 3—figure supplement 1A, B, Video 3**). Increased intracellular calcium dynamics was observable as early as 16hpf, concomitant with increased H₂O₂, but prior to onset of *hai1a* phenotypes (**Figure 3G, H, Video 4**). Release of calcium from intracellular stores is regulated by IP₃ receptors located on the endoplasmic reticulum. The frequency and number of calcium flashes in the trunk and tail of *hai1a* mutants are reduced by treatment with the IP₃R inhibitor, 2-APB compared to control (**Figure 3C, D, F, Figure 3—figure supplement 1C, D, Video 5**). Reducing calcium flashes in *hai1a* mutant embryos with 2-APB also significantly reduced H₂O₂ levels (**Figure 3I, J, Figure 3—figure supplement 1E**) and partially reduced inflammation; however, the epidermal defects were not noticeably rescued (imaged by DIC (Differential Interference Contrast) or labelled with the TP63 antibody) (**Figure 3I–K**). We observed similar reduction in neutrophil inflammation, but not rescue of epidermal defects, in *hai1a* mutants treated with thapsigargin, which inhibits the replenishment of ER calcium stores by SERCA (**Figure 3K, Figure 3—figure supplement 1F, G**). This suggests, in *hai1a* mutants, that IP₃R-dependent calcium flashes activate Duox, flooding the epidermis with H₂O₂ and leading to inflammation.

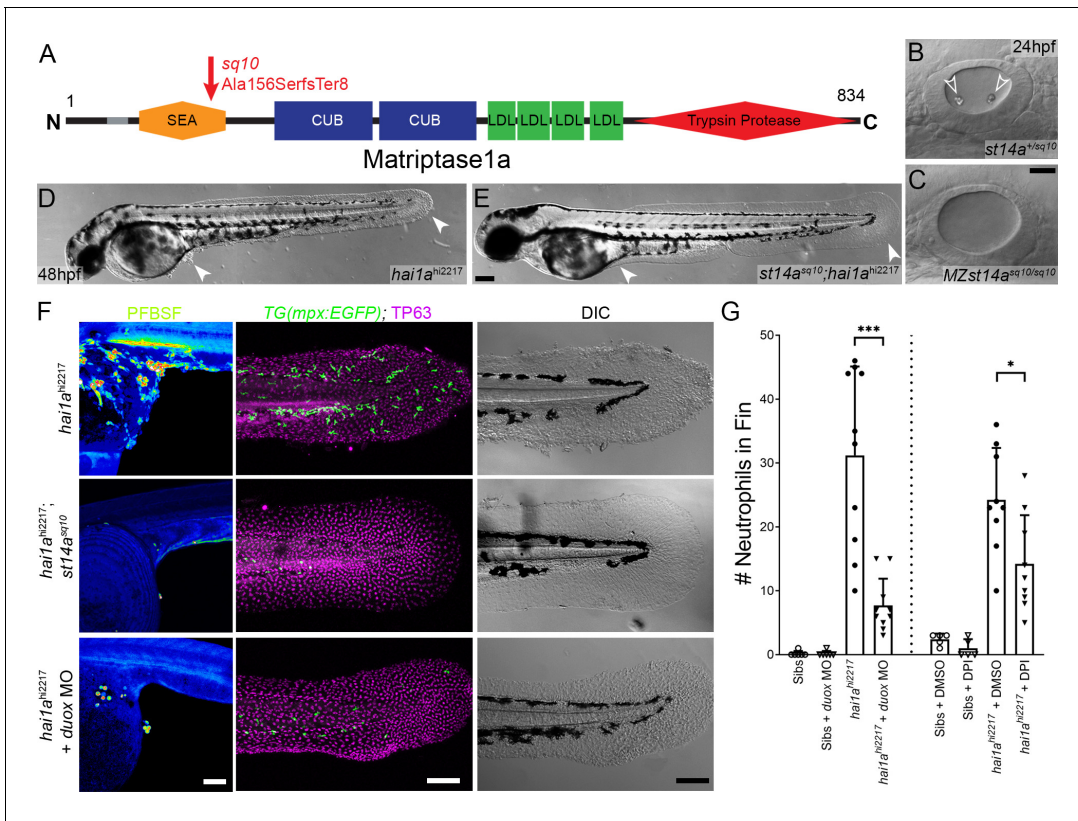


Figure 2. Loss of Matriptase1a or Duox1 reduces H₂O₂ and neutrophils in *hai1a* mutants. (A) Schematic of the Matriptase1a protein with domains given and transmembrane domain as grey line. Location and nature of the *sq10* allele given by red arrow. (B, C) Lateral DIC (Differential Interference Contrast) images of *st14a*^{+/sq10} (B) and MZ *st14a*^{sq10} (C) otic vesicles at 24hpf showing absence of otoliths (arrowheads in B) in the maternal zygotic *st14a* mutants. (D, E) Lateral DIC images of *hai1a*^{hi2217} single mutant (D) and *st14a*^{sq10}; *hai1a*^{hi2217} double mutant (E) at 48hpf highlighting rescue of epidermal aggregates and fin morphology (arrowheads) in the double mutants. (F) Projected confocal images of pentafluorobenzenesulfonyl fluorescein (PFBSF) staining at 24hpf (left column), TP63 (magenta), and eGFP (green) antibody staining at 48hpf (middle column) with DIC imaging (right column) for *hai1a*^{hi2217} single mutants (top row), *st14a*^{sq10}; *hai1a*^{hi2217} double mutants (middle row), and *hai1a*^{hi2217} mutants injected with 0.4 mM, *duox* MO + 0.2 mM *tp53* morpholino (bottom row). Individuals for middle and right columns were hemizygous for the *Tg(mpx:eGFP)*ⁱ¹¹⁴ transgene. (G) Counts of eGFP-positive neutrophils on the fins of *hai1a*^{hi2217}; *Tg(mpx:eGFP)*ⁱ¹¹⁴ or *Tg(mpx:eGFP)*ⁱ¹¹⁴, and either uninjected, injected with morpholino against *duox* (left side of graph), treated with 0.5% DMSO (Dimethyl sulfoxide) or 40 μM diphenyleneiodonium (DPI) (right side of graph). n = 10; t-test; ***p<0.001; *p<0.05. Scale bars: (C) = 20 μm; (E, F) = 100 μm.

The online version of this article includes the following figure supplement(s) for figure 2:

Figure supplement 1. Generation of *st14a* mutant and Duox inhibition reduces hydrogen peroxide and neutrophils in *hai1a* mutants.

Hydrogen peroxide elevates NfκB signalling in *hai1a* mutants

Increased Matriptase, Par2 activity, or hydrogen peroxide levels are known to activate NfκB signalling (Kanke et al., 2001; Sales et al., 2015; Schreck et al., 1991). We crossed the *hai1a*^{fr26} allele to the NfκB sensor transgenic line *Tg(6xHsa.NFKB:EGFP)*^{nc1}. In WT embryos, NfκB signalling was

Table 1. Prevalence of otolith and epithelial phenotypes in *hai1a* and *st14a* double mutants: p<0.0001 (Chi-squared test).

hai1a^{+/hi2217}; *st14a*^{+/sq10} ♂ × *hai1a*^{hi2217/hi2217}; *st14a*^{sq10/sq10} ♀

Observed (expected)	WT epidermis	<i>hai1a</i> epidermis	Total
Wild-type otoliths	72 (65)	60 (65)	132 (130)
No otoliths	128 (65)	0 (65)	128 (130)
Total	200 (130)	60 (130)	260

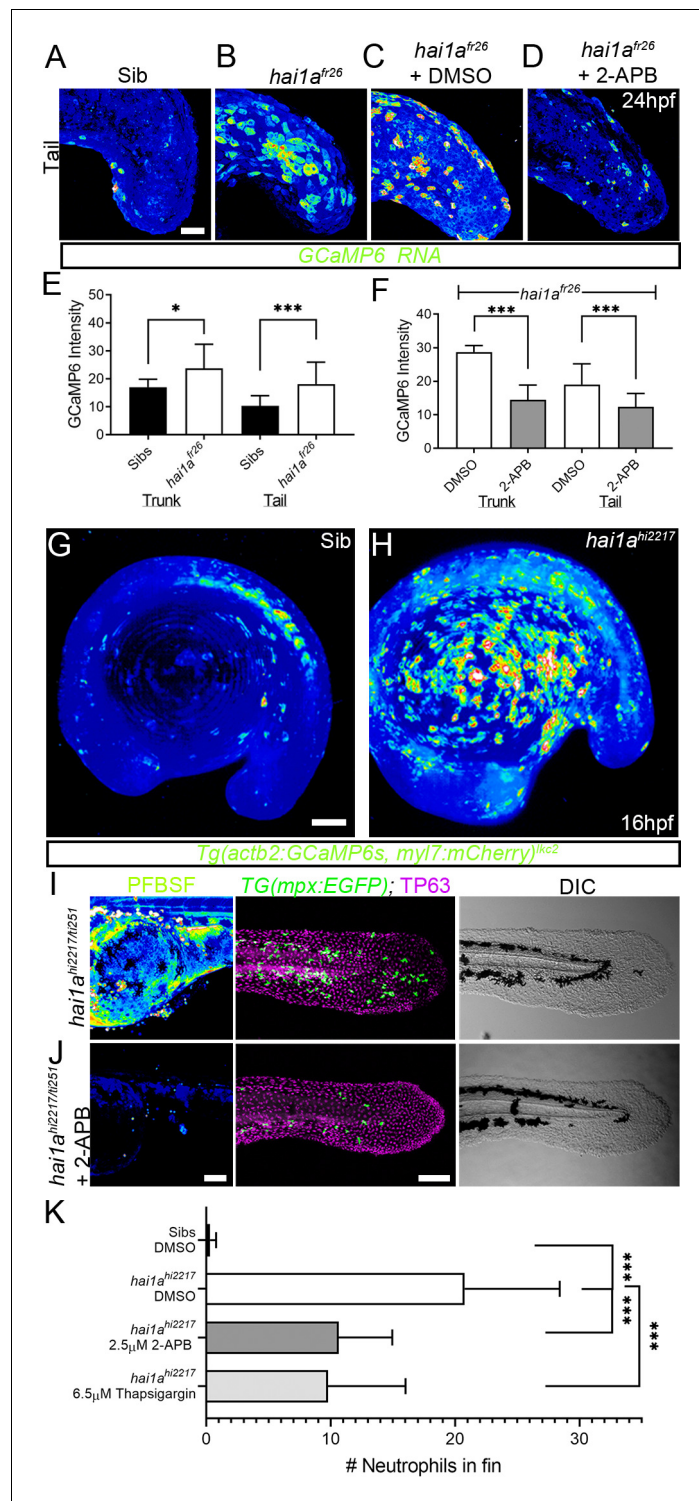


Figure 3. Calcium dynamics in *hai1a* mutants regulate H₂O₂ and inflammation. (A–D) Projected confocal images of eGFP in the tail of WT (A) or *hai1a^{fr26}*; (B–D) injected with GCaMP6s RNA, imaged at 24hpf, indicating calcium dynamics. Embryos are either untreated (A, B), treated with DMSO (C), or with 2.5 μ M 2-APB (D). Images are temporal projections of timelapse movies taken at maximum speed intervals (2 min) and projected by time. (E, F) Graphs comparing eGFP intensities from GCaMP6s RNA timelapses in trunk and tail between 24hpf WT and *hai1a^{fr26}* (E) and between *hai1a^{fr26}* treated with DMSO and 2.5 μ M 2-APB (F). n = 10; t-test; *p<0.05, ***p<0.001. (G, H) Projected light-sheet images of *Tg(actb2:GCaMP6s, myl7:mCherry)^{kkc2}* embryos indicating calcium dynamics at 16hpf of sibling (G) or *hai1a^{hi2217}* (H). Images are temporal projections of timelapse movies taken at 45 s

Figure 3 continued on next page

Figure 3 continued

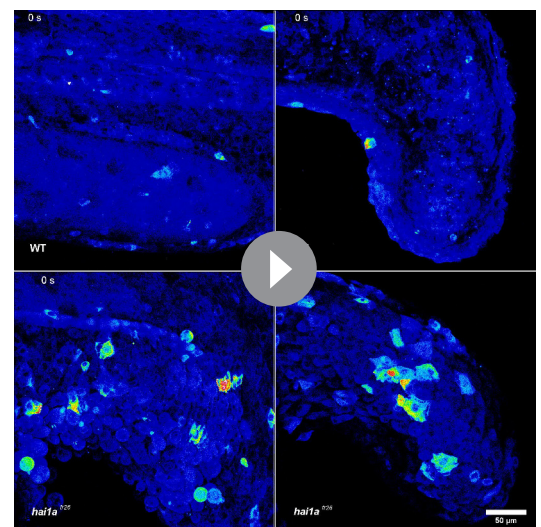
intervals and projected by time. (I, J) Pentafluorobenzenesulfonyl fluorescein (PFBSF) staining at 24hpf (left column), TP63 (magenta), and eGFP (green) antibody staining at 48hpf (middle column) with DIC imaging (right column) for *hai1a*^{hi2217/ti251} mutants (J), or *hai1a*^{hi2217/ti247} mutants treated with 2.5 μ M 2-APB (I). Individuals for middle and right columns were hemizygous for the *Tg(mpx:eGFP)*ⁱ¹¹⁴ transgene. (K) Counts of eGFP-positive neutrophils in the fins at 48hpf of *Tg(mpx:eGFP)*ⁱ¹¹⁴, or *hai1a*^{hi2217}; *Tg(mpx:eGFP)*ⁱ¹¹⁴ treated with 0.5% DMSO, 2.5 μ M 2-APB, or 6.5 μ M thapsigargin. n = 20; t-test; ***p < 0.001. Scale bars (A–D) = 50 μ m; (G, I, J) = 100 μ m. The online version of this article includes the following figure supplement(s) for figure 3:

Figure supplement 1. Thapsigargin and 2-APB reduce neutrophil inflammation but not epidermal defects in *hai1a* mutants.

mostly restricted to neuromasts at 48hpf, whilst in *hai1a* mutants we observed an increase in fluorescence at 24hpf and a strong increase at 48hpf. Fluorescence at both timepoints was noted in epidermal aggregates and fin folds, locations of strong inflammation (Figure 4A, B, Figure 4—figure supplement 1A, B). This increase in signalling in 48hpf *hai1a* mutant embryos was confirmed by qRT-PCR of the Nf κ B target gene, *nfkbiaa* (Figure 4C). Unlike calcium and H₂O₂, Nf κ B signalling is not present at early stages prior to phenotype (Figure 4—figure supplement 1C, D). To determine the extent that Nf κ B signalling accounts for the *hai1a* phenotypes, we generated a mutant in the *ikbkg* (= *ikkg* or *nemo*) gene, which encodes a scaffold protein required for activating the Nf κ B pathway (Rothwarf et al., 1998) (*ikbkg*^{sq304} Gly80ValfsTer11; Figure 4—figure supplement 1E). Crossing this mutant to *hai1a*^{hi2217} on the *Tg(mpx:eGFP)*ⁱ¹¹⁴ background realised a very strong rescue of neutrophil inflammation at 48hpf, but no improvement of *hai1a* epidermal defects (Figure 4D–I). To demonstrate that this increase in Nf κ B signalling was dependent on H₂O₂, we injected *hai1a*^{hi2217}; *Tg(6xHsa.NFKB:EGFP)*^{nc1} embryos with *duox* MO. We noted a strong reduction in Nf κ B pathway activation compared to uninjected *hai1a*^{hi2217} mutant controls (Figure 4J, K). Conversely, genetic ablation of Nf κ B signalling, through use of the *ikbkg* mutant, did not reduce H₂O₂ levels in *hai1a* mutants (Figure 4—figure supplement 1F, G). Similarly, we tested if reduction of calcium flashes could also reduce Nf κ B signalling in *hai1a* mutants using 2-APB but noticed only a slight reduction (Figure 4—figure supplement 1H, I). We propose that upon loss of Hai1a, IP₃R-mediated release of calcium activates Duox to increase H₂O₂. This acts upstream of Nf κ B pathway activation, which occurs at later stages, and is necessary for the inflammation phenotype.

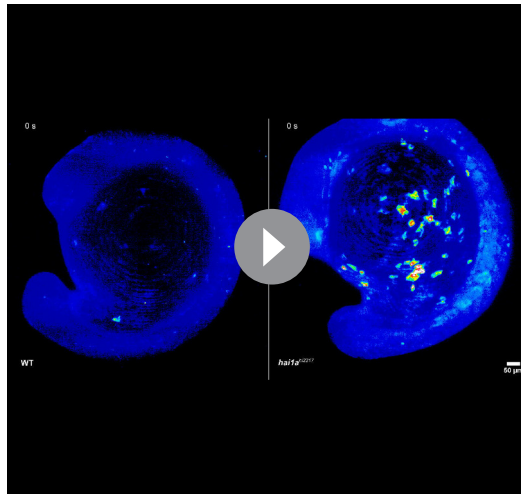
Both inflammation and epidermal aggregates of *hai1a* mutants are resolved by Gq inhibition

IP₃ is generated from cleavage of PIP₂ by Phospholipase C. The sensitivity of the *hai1a* mutants to 2-APB implies that IP₃ levels are increased and therefore there may be an increase in Phospholipase C activity. Numerous attempts to inhibit PLC in *hai1a* mutants failed, and we were unable to find a dosage window that rescued without gross embryo deformity. Hence, we tested rescue of *hai1a* mutants with YM-254890, an inhibitor of the heterotrimeric G protein alpha subunit, Gq, which directly activates PLC isoforms. We found that not only did this significantly reduce neutrophil inflammation (Figure 5D, F), but surprisingly, it also significantly rescued the epidermal defects in *hai1a* mutants, with a significant reduction in TP63-positive epidermal aggregates in the trunk and improved tail fin fold integrity at 48hpf (Figure 5A–E).



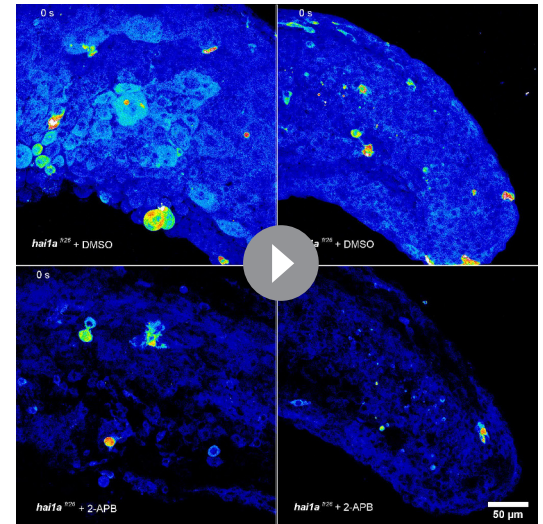
Video 3. Calcium dynamics in WT and *hai1a*^{fr26} embryos at 24hpf. Projected confocal timelapses of eGFP in the trunks (left side) and tails (right side) of a 24hpf WT (top row) and *hai1a*^{fr26} (bottom row) embryos injected with *GCaMP6s* RNA, indicating calcium dynamics. Scale bar: 50 μ m.

<https://elifesciences.org/articles/66596#video3>



Video 4. Calcium dynamics in WT and *hai1a*^{hi2217} embryos at 16hpf. Projected light-sheet timelapses of eGFP in WT (left side) and *hai1a*^{hi2217} embryos at 16hpf. Both embryos carried the *Tg(actb2:GCaMP6s, myl7:mCherry)^{kc2}* transgene reporting calcium dynamics, which were higher in the *hai1a* mutant, particularly over the yolk. Images were taken every 45 s for 19 min. Scale bar: 50 μ m.

<https://elifesciences.org/articles/66596#video4>



Video 5. Calcium dynamics in DMSO and 2-APB-treated *hai1a*^{fr26} embryos at 24hpf. Projected confocal timelapses of eGFP signal in the trunks (left side) and tails (right side) of 24hpf *hai1a*^{fr26} embryos injected with *GCaMP6s* RNA and treated with 0.03% DMSO (top row) and 2.5 μ M 2-APB (bottom row), indicating reduced calcium dynamics following 2-APB treatment. Scale bar: 50 μ m.

<https://elifesciences.org/articles/66596#video5>

PMA treatment phenocopies the *hai1a* mutant

As IP₃R inhibition only blocks inflammation in *hai1a* mutants, but an inhibitor of a PLC activator (Gq) additionally reduces the epidermal defects, we considered that diacyl glycerol (DAG) might contribute to the epidermal defects as the second product of PIP₂ cleavage (along with IP₃). Indeed, treating WT embryos from 15hpf to 24hpf with 125 ng/ml phorbol 12-myristate 13-acetate (PMA), a DAG analogue, resulted in embryos with striking similarities to strong *hai1a* mutants, including a thin or absent yolk sac extension, lack of head straightening, lack of lifting the head off the yolk, and multiple epidermal aggregates on the skin (**Figure 6A–C**). These aggregates were due, at least partially, to displacement of basal keratinocytes as shown by TP63 staining where the basal keratinocyte nuclei lost their uniform distribution (**Figure 6D, E**). Treatment from 24hpf to 48hpf with 125 ng/ml PMA led to a fin defect similar to the dysmorphic *hai1a* mutant fin (**Figure 6F, G**). It has been shown that the basal keratinocytes in *hai1a* lose their epithelial nature and adopt a partially migratory phenotype (**Carney et al., 2007; Video 6**). We treated *Tg(krtt1c19e:lyn-tdtomato)^{sq16}* larvae (**Lee et al., 2014**) with 37.5 ng/ml PMA for 12 hr and imaged the basal epidermis at 3dpf by light-sheet time-lapse. Whilst the DMSO-treated transgenic larvae had very stable keratinocyte membranes and shape, PMA treatment led to a less stable cell membrane topology and dynamic cell shape, similar to *hai1a* mutants (**Figure 6H, Videos 7 and 8**). Kymographs taken from **Video 7** highlighted both the more labile and weaker cell membrane staining following PMA treatment (**Figure 6I**). The potency of PMA was dependant on region and reduced with age.

Most PMA-treated *Tg(mpx.eGFP)ⁱ¹¹⁴* larvae at 48hpf also had more neutrophils in the epidermis than untreated controls, which were highly migratory (**Figure 6F–G, J–K', Video 8**). We determined H₂O₂ levels in PMA-treated embryos using PFBSF staining and found that it was significantly increased in both trunk and tail at 24hpf (**Figure 6L–O, R**). In contrast, when we treated *GCaMP6s* RNA-injected embryos with PMA, we failed to see an increase in calcium flashes, as seen in *hai1a* (**Figure 6P, Q, S**). To see if the heightened H₂O₂ and inflammation was also correlated with increased NfκB signalling, we treated *Tg(6xHsa.NFKB:EGFP)^{nc1}* embryos with 125 ng/ml PMA. There

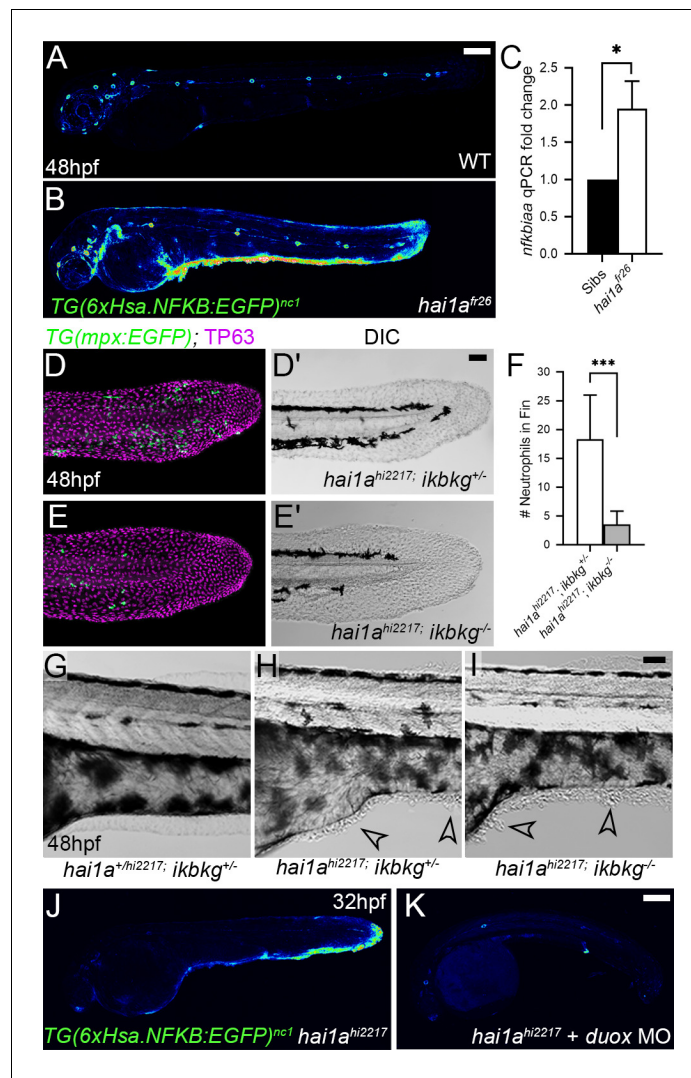


Figure 4. NfκB signalling is elevated in *hai1a* mutants and is necessary for neutrophil inflammation. (A, B) Lateral confocal projections of *Tg(6xHsa.NFKB:EGFP)^{nc1}* embryos reporting NfκB signalling levels at 48hpf for WT (A) and *hai1a^{fr26}* (B). (C) qPCR of cDNA levels of NfκB target gene *nfkbiaa* in *hai1a^{fr26}* vs. sibs at 48hpf. n = 3, 200 embryos pooled in each, t-test *p < 0.05. (D–E') Projected confocal images of the tail fins of 48hpf *Tg(mpx:eGFP)ⁱ¹⁴; hai1a^{hi2217}* embryos, immunostained for TP63 (magenta) and eGFP (green) with corresponding DIC image (D', E'). Embryos were either mutant for *ikbkg* (*ikbkg^{sq304}*, E–E') or heterozygous (*ikbkg^{+/sq304}*, D–D'). (F) Counts of eGFP-positive neutrophils in the fins at 48hpf of *hai1a^{hi2217}; ikbkg^{+/sq304}* and *hai1a^{hi2217}; ikbkg^{sq304}*. Embryos were hemizygous for *Tg(mpx:eGFP)ⁱ¹⁴*. n = 9; t-test; ***p < 0.001. (G–I) Lateral DIC images of the trunk of *hai1a^{+/hi2217}; ikbkg^{+/sq304}* (G), *hai1a^{hi2217}; ikbkg^{+/sq304}* (H), and *hai1a^{hi2217}; ikbkg^{sq304}* (I). Loss of IKKKG does not rescue epidermal defects of *hai1a* mutants (arrowheads). (J, K) Lateral confocal projections of *Tg(6xHsa.NFKB:EGFP)^{nc1}* embryos reporting NfκB signalling levels at 32hpf of *hai1a^{hi2217}* un.injected (J) or injected with *duox* MO (K). Loss of H₂O₂ reduces NfκB signalling levels in *hai1a* mutants. Scale bars: (A, K) = 200 μm; (D', I) = 50 μm.

The online version of this article includes the following figure supplement(s) for figure 4:

Figure supplement 1. NfκB signalling is elevated in *hai1a* mutants, and mutation of *ikbkg* rescues neutrophil inflammation.

was a robust increase in fluorescence, indicating that PMA activates the NfκB pathway (Figure 6T, U).

The phenocopy and the rescue of *hai1a* by PMA and Gq inhibition respectively imply that DAG is elevated in *hai1a* mutants. Elevated cellular DAG leads to relocalisation of Protein Kinase C isoforms to the plasma and nuclear lipid membranes where they bind DAG and become activated. Using a

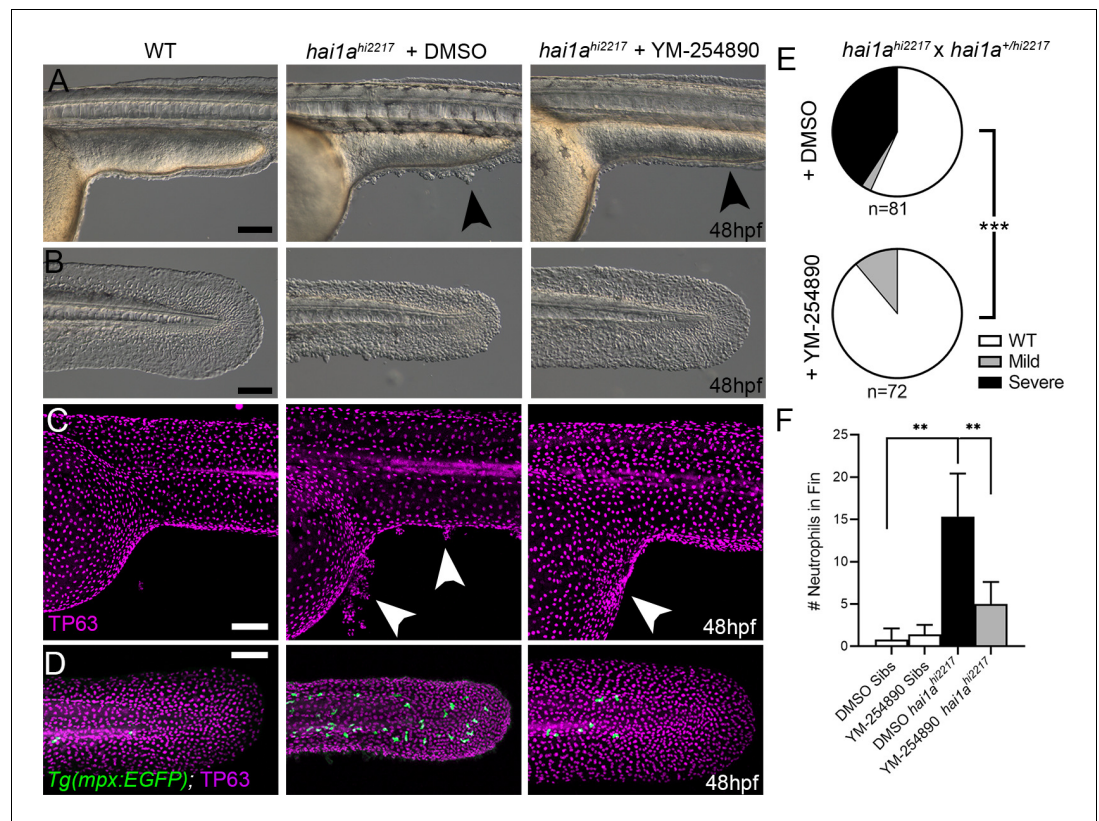


Figure 5. Gq inhibition rescues both epidermal and inflammation phenotypes of *hai1a* mutants. (A–D) Lateral images of ventral trunk and tail at 48hpf for WT (left panels), *hai1a*^{hi2217} treated with 0.5% DMSO (middle panels), and *hai1a*^{hi2217} treated with 32 μ M YM-254890 (right panels). DIC micrographs are shown in (A, B), whilst projected confocal images are shown in (C, D), where embryos are immunostained for TP63 (C, D; magenta) and eGFP (D; green). Embryos in (D) are hemizygous for *Tg(mpx:eGFP)*ⁱ¹¹⁴. Arrowheads indicate region of aggregate formation lost upon treatment with Gq inhibitor YM-254890. (E) Pie charts showing proportion of embryos with no (WT; white), mild (grey) or severe (black) *hai1a* mutant epidermal phenotypes. Embryos were derived from *hai1a*^{hi2217/hi2217} \times *hai1a*^{+/hi2217} crosses and assayed at 48hpf. Clutches treated with 0.5% DMSO (upper pie chart) were compared to those treated with 32 μ M YM-254890 (lower pie chart) by Chi-squared analysis. *** p <0.001; n = 72. (F) Graph of counts of eGFP-positive neutrophils in the fins at 48hpf of *Tg(mpx:eGFP)*ⁱ¹¹⁴, or *hai1a*^{hi2217}; *Tg(mpx:eGFP)*ⁱ¹¹⁴ treated with 0.5% DMSO, or 32 μ M YM-254890. n = 6; Mann–Whitney test; ** p <0.01. Scale bars: (A–D) = 100 μ m.

GFP-tagged PKC δ fusion protein (Sivak et al., 2005), we showed that in the WT embryo there was largely diffuse cytoplasmic PKC δ -GFP signal, however, it translocated to plasma and nuclear membranes in *hai1a* mutants, indicating increased levels of DAG (Figure 7A, B, Figure 7—figure supplement 1A, B). This is indeed relevant to the epidermal defects, as treatment of *hai1a*^{hi2217} embryos with the PKC inhibitor, GFX109203, reduced the epidermal aggregates and disruption of fin morphology as imaged by DIC or immunostaining for TP63 (Figure 7C–H). Neutrophil inflammation in the epidermis was somewhat reduced, but not to a significant degree (Figure 7E–I). Thus, these experiments strongly suggest that epithelial defects of *hai1a* are due to DAG generation and PKC activation.

Elevated MAPK signalling generates epithelial defects in *hai1a*

We next sought to determine which pathways downstream of PKC are responsible for the epidermal defects. The MAPK pathway is a major target pathway of multiple PKC isoforms, and activation of this pathway in zebrafish epidermis has previously been shown to induce papilloma formation which have very similar attributes to *hai1a* mutant aggregates (Chou et al., 2015). Although whole embryo western analysis of *hai1a* mutants failed to show an overall increase in pERK (Armistead et al.,

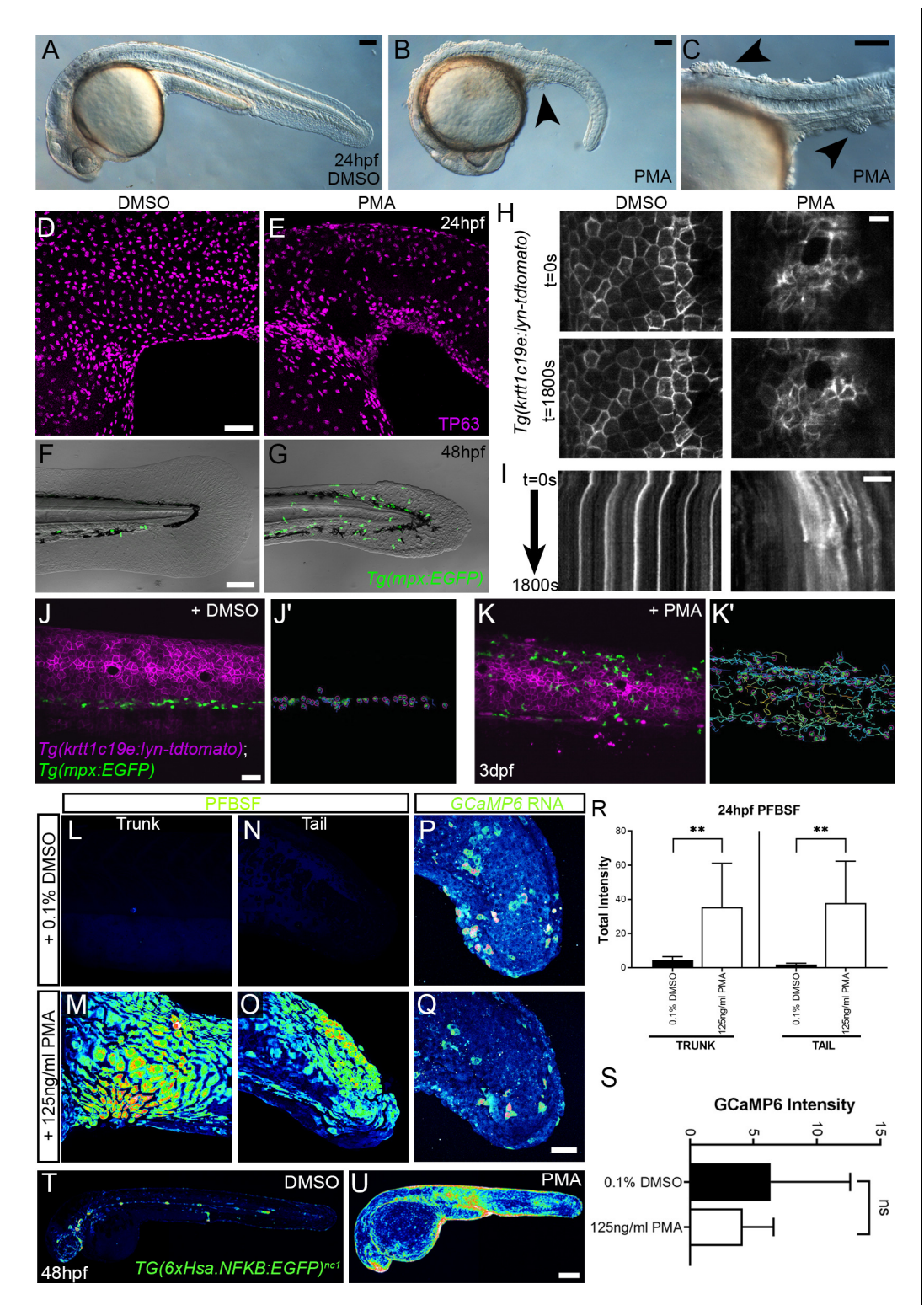


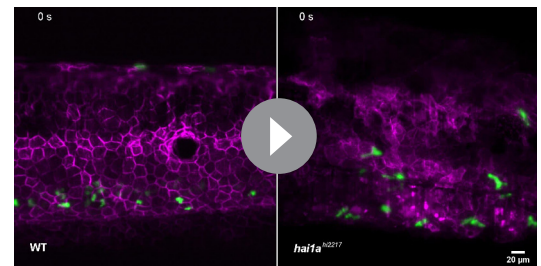
Figure 6. Phorbol 12-myristate 13-acetate (PMA) induces epidermal aggregates, motility, H₂O₂, NfκB, and inflammation. (A, B) Lateral micrographs of embryos treated with DMSO (A) or 125 ng/ml PMA (B, C) showing generation of epidermal aggregates (arrowheads). (D, E) Projected confocal images of the trunk of 24hpf WT embryos treated with 0.1% DMSO (D) or 125 ng/ml PMA (E) and immunostained for TP63 (magenta), showing aggregation of TP63-positive cells. (F, G) Projected confocal images superimposed on DIC image of the tail of 48hpf *Tg(mpx:eGFP)¹¹⁴* embryos treated with 0.1% DMSO (F) or 125 ng/ml PMA (G) showing fin defect and

Figure 6 continued

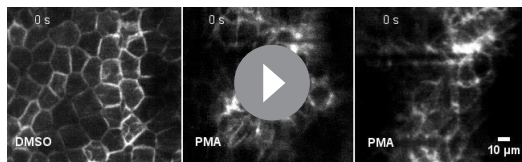
activation of eGFP-positive neutrophils (green, **G**). (**H**, **I**) Single timepoint images at $t = 0$ (top panels, **H**) and $t = 1800$ s (lower panels, **H**) and kymographs (**I**) derived from light-sheet movies (**Video 7**) of the epidermis of 3dpf *Tg(krtt1c19e:lyn-tdtomato)^{sq16}* larvae treated with 0.1% DMSO (left panels) or 37.5 ng/ml PMA (right panels) showing the lack of membrane stability following PMA treatment. (**J–K'**) Single frames (**J**, **K**) and tracks of eGFP-positive neutrophils (**J'**, **K'**) from light-sheet (**Video 8**) showing neutrophils labelled by eGFP and basal keratinocyte cell membranes labelled by lyn-tdTomato in the trunk of a 3dpf *Tg(krtt1c19e:lyn-tdtomato)^{sq16}* larva treated with 0.1% DMSO (**J**, **J'**) or 37.5 ng/ml PMA (**K**, **K'**) for 18 hr, and imaged every 20 s for 30 min. Track colour in (**J'**, **K'**) denotes mean velocity (dark blue 0.0 – red 0.2). (**L–O**) Projected lateral confocal views of pentafluorobenzenesulfonyl fluorescein (PFBSF) staining of 24hpf WT embryos treated with 0.1% DMSO (**L**, **N**) or 125 ng/ml PMA (**M**, **O**) showing elevation of H_2O_2 in the trunk (**L**, **M**) and tail (**N**, **O**). (**P**, **Q**) Projected confocal images of eGFP in the tail at 24hpf of WT injected with *GCaMP6s* RNA, treated with DMSO (**P**), or with 125 ng/ml PMA (**Q**). Images are temporal projections of timelapse movies taken at maximum speed intervals (2 min) and projected by time. (**R**) Plot of PFBSF fluorescent staining intensity of WT embryos treated with 0.1% DMSO or 125 ng/ml PMA in the trunk and tail. $n = 6$; ANOVA with Bonferroni post-test $**p < 0.01$. (**S**) Graph comparing eGFP intensities from 24hpf *GCaMP6s* RNA timelapses in tail following treatment with DMSO and 125 ng/ml PMA. $n = 10$; t-test. (**T–U**) Lateral confocal projections of *Tg(6xHsa.NFKB:EGFP)^{nc1}* embryos reporting NfκB signalling levels at 48hpf in WT treated with DMSO (**T**) and WT treated with 125 ng/ml PMA (**U**). Scale bars: (**A**, **B**, **C**, **F**) = 100 μm; (**D**, **J**, **Q**) = 50 μm; (**H**, **I**) = 20 μm; (**U**) = 200 μm.

2020), we performed wholemount immunofluorescent analysis in case there was only a localised effect. Indeed, we observed a significant and localised increase in cytoplasmic pERK immunoreactivity (phospho-p44/42 MAPK (Erk1/2) (Thr²⁰²/Tyr²⁰⁴)) in the regions of epidermal aggregate formation in *hai1a* mutants and in PMA-treated embryos, including under the yolk at 24hpf and in the fins at 24hpf and 48hpf (**Figure 8A–K**, **Figure 8—figure supplement 1A–F**). There was no increase in total ERK levels in the mutant (**Figure 8—figure supplement 1M, N**). Increased pERK was seen in both the cytoplasm and nucleus of TP63-positive cells but was only increased in the nucleus of periderm cells (**Figure 8E–E'**, **Figure 8—figure supplement 1D**). To establish that this is an early marker of aggregate formation, and not a sequela, we stained *hai1a* mutant embryos at earlier timepoints. We found that at 16hpf regions of the epidermis have pERK staining before overt aggregation formation (**Figure 8G–H**), whilst nascent aggregates also contain pERK staining which increases in number over time (**Figure 8—figure supplement 1G–L**).

To determine if elevated pERK is causative of epidermal defects, we attempted to rescue using pERK inhibitors. Initially we used PD0325901; however, this appeared to give fin fold deformities, even in WT embryos (**Anastasaki et al., 2012**), precluding ability to assess rescue in *hai1a*, although there was a noticeable reduction in epidermal aggregates forming under the yolk-sac extension (data not shown). Instead, we tried U0126 and CI-1040, other well-known pERK inhibitors (**Allen et al., 2003**; **Favata et al., 1998**). Both inhibitors showed a significant reduction in *hai1a* mutant epidermal aggregates under the yolk, and restoration of the overall and tail epithelial morphology, with embryos showing a *hai1a* phenotype class significantly reduced (**Figure 9A–G**, **Figure 9—figure supplement 1A–F**). Similarly, the epidermal defects of the trunk, yolk, and tail following PMA treatment were also ameliorated by concomitant U0126 treatment (**Figure 9H, I**, **Figure 9—figure supplement 1G, H**). Rescue of aggregates and tail morphology following PMA treatment or in *hai1a* mutants could be visualised by immunolabelling TP63 in basal keratinocyte nuclei (**Figure 9J–O**,

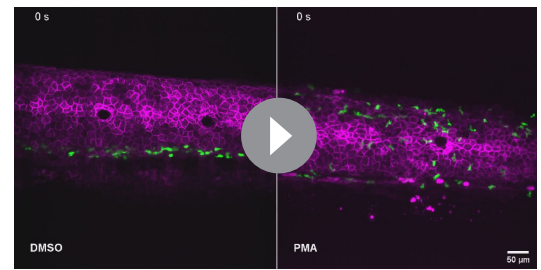


Video 6. Basal keratinocyte membrane and neutrophil dynamics in 3dpf wild-type and *hai1a^{hi2217}* larvae carrying the *Tg(krtt1c19e:lyn-tdtomato)^{sq16}* and *Tg(mpx:eGFP)¹¹⁴* transgenes. Projected light-sheet timelapses of the trunk of 3dpf WT (left) and *hai1a^{hi2217}* (right) larvae with neutrophils and basal keratinocyte membranes labelled by eGFP and lyn-tdTomato, respectively. Both larvae carried the *Tg(krtt1c19e:lyn-tdtomato)^{sq16}*; *Tg(mpx:eGFP)¹¹⁴* transgenes. The *hai1a* mutants have highly dynamic neutrophils and keratinocyte membrane dynamics. Scale bar: 20 μm. <https://elifesciences.org/articles/66596#video6>



Video 7. Basal keratinocyte membranes in DMSO and phorbol 12-myristate 13-acetate (PMA)-treated 3dpf *Tg(krtt1c19e:lyn-tdtomato)^{sq16}* larvae. Zoomed projected light-sheet timelapses of basal keratinocyte membranes labelled by lyn-tdTomato in the trunk of 3dpf *Tg(krtt1c19e:lyn-tdtomato)^{sq16}* larvae treated with 0.1% DMSO (left) and 37.5 ng/ml PMA (middle and right) for 18 hr. Membranes are stable in DMSO-treated larvae but were dynamic in PMA-treated larvae. Images were captured every 20 s. Scale bar: 10 μ m.

<https://elifesciences.org/articles/66596#video7>



Video 8. Neutrophils and basal keratinocyte membranes in DMSO and phorbol 12-myristate 13-acetate (PMA)-treated 3dpf *Tg(krtt1c19e:lyn-tdtomato)^{sq16}; Tg(mpx:eGFP)ⁱ¹¹⁴* larvae. Lateral projection of light-sheet timelapse of neutrophils labelled by eGFP and basal keratinocyte cell membranes labelled by lyn-tdTomato in the trunks of 3dpf *Tg(krtt1c19e:lyn-tdtomato)^{sq16}* larva treated with 0.1% DMSO (left) and 37.5 ng/ml PMA (right) for 18 hr. PMA treatment leads to slightly dynamic cell membranes and motile neutrophils. Images were captured every 20 s for 30 min. Scale bar: 50 μ m.

<https://elifesciences.org/articles/66596#video8>

Figure 9—figure supplement 1I, J. Initiating U0126 treatment later at 26hpf led to only a partial rescue, indicating that the epidermal phenotypes were likely due to sustained pERK activation (**Figure 9—figure supplement 1K–M**).

Treatment with U0126 did not significantly reduce neutrophil inflammation of *hai1a* mutants or PMA treatment (**Figure 9L–P**). This suggests that the inflammation phenotype is not simply a consequence of the epidermal defects. Furthermore, dye penetration assays showed that the epithelial barrier was not globally and overtly compromised in *hai1a*, underscoring that inflammation is not simply a consequence of epithelial defects (**Figure 9—figure supplement 2A–H**). It has been shown that the epidermal defects in *hai1a* are associated with loss of E-cadherin from adherens junctions (**Carney et al., 2007**). As there was a rescue of the epithelial phenotype following pERK inhibition, we looked at the status of the adherens junction marker β -catenin. Whilst the WT basal epidermal cells of the 48hpf tail showed strong staining at the membrane, *hai1a* mutants and PMA-treated embryos showed a significant loss of β -catenin at the membrane and increase in the cytoplasm (**Figure 9Q–V, Y, Z**). Treatment of *hai1a* mutants with U0126 restored the membrane localisation of β -catenin (**Figure 9W, X, AA**).

Phosphorylation of cytoplasmic RSK by pERK leads to loss of E-cadherin at the *hai1a* keratinocyte membrane

As increased pERK appeared to contribute strongly to loss of adherens junctions and removal of E-cadherin/ β -catenin from the membrane, we sought to determine how pERK signalling might affect adherens junctions. We predicted that this would occur through a cytoplasmic target of pERK as we have previously shown that there is no transcriptional downregulation of E-cadherin levels in *hai1a*, making a nuclear transcription factor target less likely to be relevant (**Carney et al., 2007**). The p90RSK family of kinases represents direct cytoplasmic targets of Erk1/2 phosphorylation which regulate cell motility, and thus were good candidates for mediators disrupting cell-cell adhesion (**Čáslavský et al., 2013; Tanimura and Takeda, 2017**). We determined that at least RSK2a (=p90RSK2a, encoded by *rps6ka3a*) is expressed in basal keratinocytes at 24hpf (**Figure 10A, B**). To gauge if there was an alteration in phosphorylation of RSK family members in the epidermis of *hai1a* mutants, we used an antibody which detects a phosphorylated site of mouse p90RSK (Phospho-Thr³⁴⁸). This site is phosphorylated in an ERK1/2-dependent manner (**Romeo et al., 2012**). We noticed a substantial increase in cytoplasmic signal in both *hai1a* mutants and PMA-treated embryos. Where p90RSK-pT³⁴⁸ signal was largely nuclear in both basal and periderm cells in WT, it was more broadly observed in *hai1a* mutant fins, with an increase in the cytoplasm leading to a more uniform staining (**Figure 10C–D**). This increase in cytoplasmic levels of p90RSK-pT³⁴⁸ was observable at 17hpf prior to epithelial defects (**Figure 10—figure supplement 1A–C**). p90RSK cytoplasmic signal

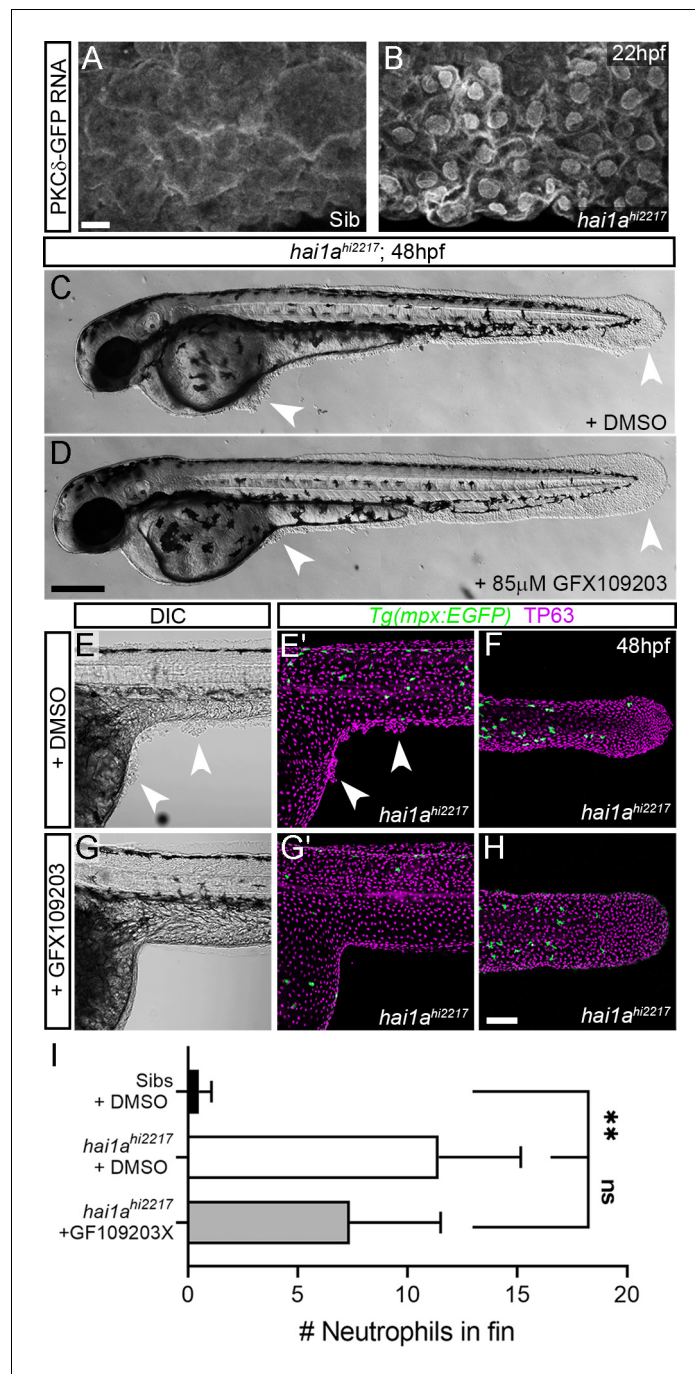


Figure 7. Inhibition of PKC rescues epidermal defects of *hai1a*. (A, B) Confocal images of the ventral fin of 22hpf sibling (A) or *hai1a^{hi2217}* (B) embryos injected with RNA encoding PKC δ -GFP. Mostly cytoplasmic distribution in sibling was relocated to cell and nuclear membranes in *hai1a* mutants. (C, D) Lateral brightfield images of 48hpf *hai1a^{hi2217}* larvae treated with 0.5% DMSO (C) or 85 μ M GFX109203 (D). Epidermal aggregates and fin deterioration are rescued by the PKC inhibitor (arrowheads). (E–H) DIC (E, G) and projected confocal images (E', G', F, H) of *hai1a^{hi2217}*; *Tg(mpx:eGFP)¹¹⁴* trunk at 24hpf (E–E', G–G') and tail at 48hpf (F, H), either treated with 0.5% DMSO (E–F) or 85 μ M GFX109203 (G–H). Embryos are immunostained for TP63 (magenta) and eGFP (green), highlighting rescue of epidermal phenotype and partial rescue of neutrophils by GFX109203. (I) Counts of eGFP-positive neutrophils in the fins at 48hpf of *Tg(mpx:eGFP)¹¹⁴*, or *hai1a^{hi2217}*; *Tg(mpx:eGFP)¹¹⁴* treated with 0.5% DMSO or 85 μ M GFX109203. n = 8; ANOVA, Dunn's multiple comparisons; **p<0.01. Scale bars: (A) = 10 μ m; (D) = 200 μ m; (H) = 100 μ m.

The online version of this article includes the following figure supplement(s) for figure 7:

Figure 7 continued on next page

Figure 7 continued

Figure supplement 1. Relocation of PKC δ -GFP to membranes in *hai1a* mutants.

was lost upon U0126 and GFX109203 treatments, showing that it was pERK and PKC dependant (**Figure 10E, E'**, **Figure 10—figure supplement 1D, E**). Similarly, increased cytoplasmic p90RSK-pT³⁴⁸ was observed following PMA treatment which was reduced by co-treatment with U0126 (**Figure 10F–H'**). The increase in cytoplasmic p90RSK-pT³⁴⁸ signal, and its reduction by U0126, was significant in both *hai1a* mutants and PMA-treated embryos (**Figure 10I, J**).

If phosphorylation of an RSK protein is required for mediating the pERK epidermal defects in *hai1a* mutants, then inhibition of RSK should rescue the epidermal defects. As morpholino-targeted inhibition of *rps6ka3a* was unsuccessful, we employed established pan-RSK inhibitors BI-D1870 and dimethyl fumarate (**Andersen et al., 2018; Sapkota et al., 2007**). Dimethyl fumarate treatment reduced the extent of cytoplasmic p90RSK-pT³⁴⁸ in *hai1a* (**Figure 10—figure supplement 1F, G**). We noted that both inhibitors were able to reduce epidermal aggregates in *hai1a* mutants and restore fin morphology when visualised by DIC or TP63 immunofluorescence (**Figure 10K–N, Figure 10—figure supplement 1H, I, K, L**). Reduction of mutant phenotype classes was significant at both 24hpf and 48hpf (**Figure 10—figure supplement 1J**). We then assayed if RSK inhibition can reduce the aberrant cytoplasmic E-cadherin staining in *hai1a* mutant basal keratinocytes and observed that dimethyl fumarate treatment restored membrane localisation of E-cadherin in the mutants (**Figure 10O–Q'**). Thus, phosphorylation of RSK proteins is altered in *hai1a* mutants, and their inhibition appears to restore E-cadherin to the membrane and reduce epidermal aggregate formation.

Discussion

There are a number of similarities between loss of Hai1a in zebrafish and overexpression of Matriptase in the mouse epidermis, including inflammation, hyperproliferation, and enhanced keratinocyte motility, suggesting conservation of downstream pathways. What the conserved ancestral role of the Matriptase-Hai1 might have been is unclear. Matriptase dysregulation in the mouse is associated with cancer progression (**Martin and List, 2019**). Tumours have long been considered to represent non-healing wounds, and the cellular- and tissue-level phenotypes of *hai1a* have similarities to tumours. Epidermal cells in zebrafish transformed by MAPK activation both promote and respond to inflammation through similar mechanisms to wound responses (**Feng et al., 2010; Schäfer and Werner, 2008**). Further, tissue damage of the zebrafish epidermis perturbs osmolarity and releases nucleotides, leading to inflammation and epithelial cell motility, with the resulting phenotypes strikingly similar to *hai1a* mutants (**de Oliveira et al., 2014; Enyedi and Niethammer, 2015; Gault et al., 2014; Hatzold et al., 2016**). Indeed, the tissue responses initiated by loss of zebrafish Hai1a have been previously suggested to represent an early injury response (**Schepis et al., 2018**), whilst PAR2 synergises with P2Y purinergic and EGF receptors to promote cell migration in scratch assays (**Shi et al., 2013**). Thus our analysis supports the previous hypothesis of the Hai1-Matriptase system as a component of tissue injury responses (**Schepis et al., 2018**), which, if inappropriately activated, promotes carcinoma.

The various molecular pathways known to be activated by Matriptase have not been fully delineated or integrated. Par2 has previously been shown to be required for the *hai1a* phenotype in zebrafish and contributes to the phenotypes of Matriptase overexpression in the mouse. Exactly which heterotrimeric G-protein Par2 is activating in vivo and how this links to phenotypes has not been identified. Our analyses allow us to propose a pathway downstream of Par2 which accounts for both the inflammatory and the epidermal phenotypes (**Figure 11**). Firstly, inhibition of Gq rescued both the inflammation and epithelial defects. PAR2 activation of Gq has been documented to occur in many cell types including keratinocytes, where inhibition of Gq and PKC reduces PAR2-mediated Nfkb signalling (**Böhm et al., 1996; Goon Goh et al., 2008; Macfarlane et al., 2005**). Although we were unable to rescue *hai1a* phenotypes with a PLC inhibitor due to toxicity, genetic sensors demonstrated increased levels of Ca⁺⁺ and DAG in *hai1a* epidermis. Our analysis demonstrated that the different products of PIP2 hydrolysis appear to invoke the two main *hai1a* phenotypes to different

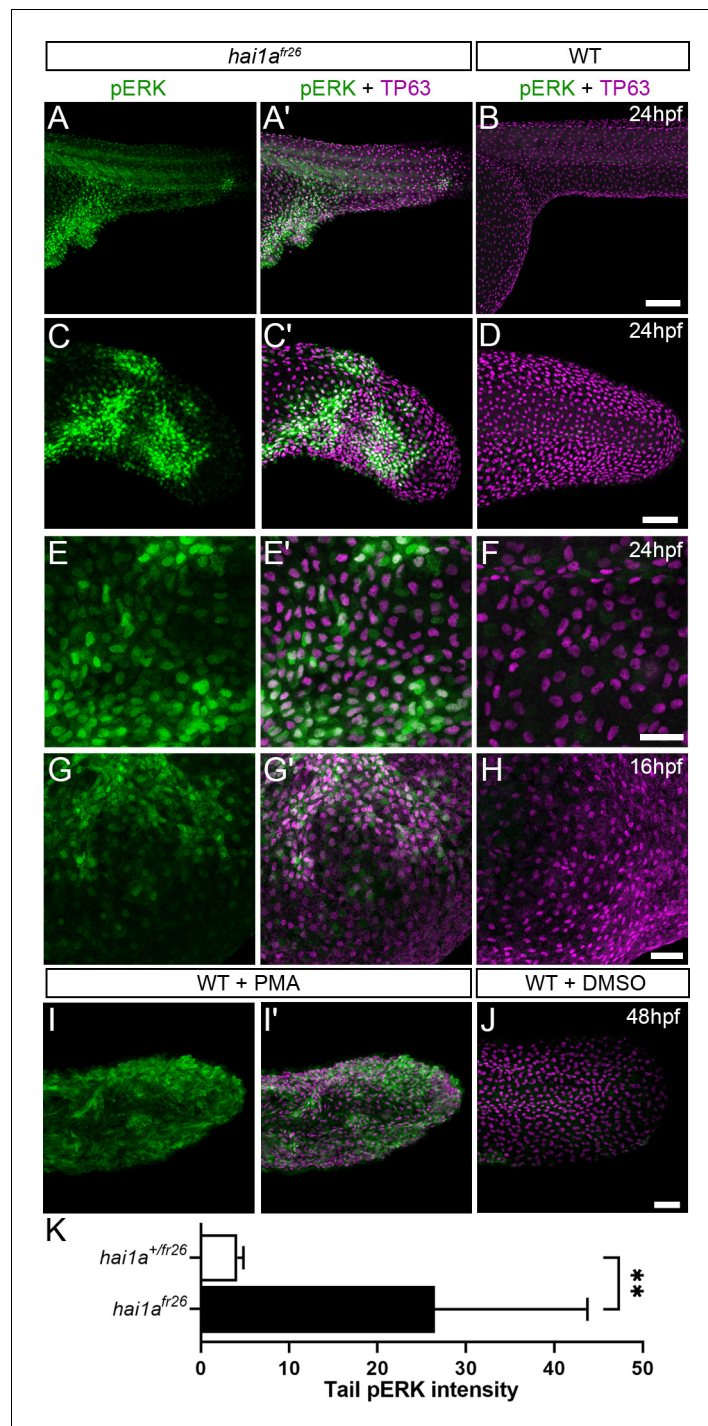


Figure 8. Elevation of pERK levels in phorbol 12-myristate 13-acetate (PMA)-treated and *hai1a* mutant epidermis. (A–L) Lateral projected confocal images of trunks (A, A', B, E, E', F), yolk surface (G, G', H) and tails (C, C', D, I, I', J) of embryos immunostained for TP63 (A', B, C', D, E', F, G', H, I', J; magenta) and pERK (A, J; green) at 24hpf (A–F), 16hpf (G–H), and 48hpf (I–J). Both *hai1a*^{fr26} (A, A', C, C', E, E', G, G') and 125 ng/ml PMA-treated (I, I') embryos show increased epidermal pERK levels compared to untreated WT (B, D, F, H, J). Elevation of epidermal pERK in *hai1a*^{fr26} mutants and PMA- treated embryos is seen in the trunk (A, E) and tail (C, I) as well as in epidermis over the yolk prior to overt phenotype manifestation (G). (K) Quantification of pERK immunofluorescent intensity in the tail of 24hpf *hai1a*^{fr26} larvae compared to siblings. n = 5; Mann–Whitney test; **p<0.01. Scale bars: (B) = 100 μm; (D, H, J) = 50 μm; (F) = 20 μm.

The online version of this article includes the following figure supplement(s) for figure 8:

Figure 8 continued on next page

Figure 8 continued

Figure supplement 1. Elevation of pERK levels in phorbol 12-myristate 13-acetate (PMA)-treated and *hai1a* mutant epidermis.

extents. IP₃R-dependent calcium release in *hai1a* epidermis was required for Duox activity, high hydrogen peroxide levels, and, later, increased NfκB signalling. Reduction of these attenuated the inflammatory, but not epithelial, defects. Conversely, inhibiting the DAG receptor, PKC, rescued the epithelial phenotypes, and the inflammation slightly. The DAG analogue, PMA, phenocopied the epidermal defects of *hai1a* mutants but also increased H₂O₂, NfκB, and neutrophil inflammation, indicating that PKC activation may be sufficient, but not necessary, for inflammation. This is in line with known activation of Duox and IKK by PKC (Rigutto et al., 2009; Turvey et al., 2014). In addition, expression of activated Ras in zebrafish keratinocytes has been shown to lead to H₂O₂ release and neutrophil attraction (Feng et al., 2010). Thus, there is likely to be dual contribution to the inflammatory phenotype from IP₃ and DAG. It is important to stress however that the inflammation is not simply a result of epithelial defects or an overt loss of barrier. Firstly, we see increase in Ca⁺⁺ and H₂O₂ very early in the epidermis prior to skin defects. Secondly, barrier assays failed to conclusively show a broad increase in permeability. Finally, rescue of epithelial defects by PKC and pERK inhibition did not fully rescue the inflammation. We conclude in our model that DAG contributes to both aspects of the phenotype, but IP₃ promotes only the inflammation.

Seminal experiments in transgenic mice overexpressing Matriptase in the epidermis and treated with a DMBA/PMA regime concluded that Matriptase and PMA activate functionally similar carcinoma promoting pathways (List et al., 2005). Our subsequent analysis suggests that this would include the MAPK pathway as we see increased phosphorylated-ERK in the epidermis of both *hai1a* mutants and also PMA-treated embryos. That we can rescue the epithelial defects using a MEK inhibitor indicated that this increase in epidermal pERK is likely critical to the phenotype. The MAPK pathway is known to regulate cell motility (Tanimura and Takeda, 2017). In the zebrafish epidermis, misexpression of activated MEK2 generated papillomas with remarkable resemblance to the epidermal aggregates in *hai1a* mutants (Chou et al., 2015), and which are not overtly proliferative. In astrocytes and oesophageal or breast tumour cell lines, PAR2 stimulates migration and invasiveness through MAPK/ERK, activation of which required Gq and PIP2 hydrolysis (Jiang et al., 2004; McCoy et al., 2010; Morris et al., 2006; Sheng et al., 2019).

One of the main molecular defects defined for zebrafish *hai1a* is the removal of adherens junction proteins from the membrane (Carney et al., 2007). MAPK signalling has been shown to reduce E-cadherin expression at adherens junctions and promote cytoplasmic accumulation through phosphorylation of the effector, RSK (Čáslavský et al., 2013). Like Matriptase, activation of RSK2 is associated with tumour progression, promoting invasiveness and metastasis of glioblastomas and head and neck squamous cell carcinomas (Kang et al., 2010; Sulzmaier et al., 2016). Promotion of invasiveness has also been noted for activated RSK1, which promotes invasion of melanoma clinically as well as in vitro and zebrafish melanoma models (Salhi et al., 2015). Intriguingly, proximity protein labelling has identified p120-catenin as a target of RSK phosphorylation. This catenin promotes cell-cell adhesion by stabilising cadherins at junctions, a function inhibited by RSK phosphorylation (Méant et al., 2020). More broadly, RSK2 activity promotes cell motility through other mechanisms, including inactivation of Integrins and activation of the RhoGEF, LARG (Gawecka et al., 2012; Shi et al., 2018). Thus, we propose that pERK signalling, through RSK members, significantly contributes to dissolution of adherens junctions and the *hai1a* epidermal phenotype. We observed increased pERK in the cytoplasm and also the nucleus of keratinocytes, with comparatively more nuclear levels in periderm cells. Thus, whilst RSKs are phosphorylated by pERK, it is also likely that other cytoplasmic and also nuclear targets, such as cFos and Ets transcription factors, may also be activated, and that there are underlying transcriptional changes in *hai1a* mutants. It is not clear why pERK shows slightly different subcellular localisation patterns between the two different epidermal layers, but the two layers do respond differently to ErbB2 inhibition (Schepis et al., 2018), whilst calcium is recently described to alter nuclear shuttling of pERK (Chuderland et al., 2020).

Our model for how Matriptase invokes cellular responses is highly likely to be incomplete. Indeed, others have indicated MMPs, HB-EGF, EGFR, and AKT and are downstream of Matriptase and PAR2

function (List et al., 2005; Schepis et al., 2018; Darmoul et al., 2004; Chung et al., 2013; Rattenholl et al., 2007). Furthermore, Matriptase promotes HGF-cMet signalling in mouse (Szabo et al., 2011). We do not think that these conflict with our model but will interface with it. A number of reports have demonstrated that PI3K/AKT and MEK/ERK function in parallel downstream of PAR2 (Sheng et al., 2019; Tanaka et al., 2008; van der Merwe et al., 2009). Furthermore, there is evidence that PKC activates both MEK/ERK and EGFR independently following PAR2 stimulation, and that PI3K is activated by PAR2 via Gq (Wang and DeFea, 2006; Al-Ani et al., 2010). Cell identity, subcellular localisation, β -arrestin scaffolding, and biased agonism/antagonism are known to generate alternative downstream outputs from PAR2 (Zhao et al., 2014). To understand fully the roles of Matriptase and PAR2 in epithelial homeostasis and carcinoma, it will be critical to map how, when, and where they activate different downstream pathways.

Materials and methods

Key resources table

Reagent type (species) or resource	Designation	Source or reference	Identifiers	Additional information
Gene (<i>Danio rerio</i>)	<i>hai1a</i>	GenBank	NM_213152	= <i>spint1a</i>
Gene (<i>Danio rerio</i>)	<i>matriptase1a</i>	GenBank	NM_001040351	= <i>st14 a</i>
Gene (<i>Danio rerio</i>)	<i>duox</i>	GenBank	XM_017354273	= <i>dual oxidase</i>
Gene (<i>Danio rerio</i>)	<i>ikbkg</i>	GenBank	NM_001014344	= <i>ikky</i> = <i>nemo</i>
Gene (<i>Danio rerio</i>)	<i>nfkbiaa</i>	GenBank	NM_213184	= <i>ikbaa</i>
Gene (<i>Danio rerio</i>)	<i>rps6ka3a</i>	GenBank	NM_212786	= <i>RSK2a</i> = <i>p90RSK2a</i>
Gene (<i>Danio rerio</i>)	<i>tp63</i>	GenBank	NM_152986	= <i>delta Np63</i>
Strain, strain background (<i>Escherichia coli</i>)	Top10	Invitrogen	C404010	Chemical competent cells
Strain, strain background (<i>Danio rerio</i>)	AB	ZIRC		Wild-type strain
Strain, strain background (<i>Danio rerio</i>)	TL	ZIRC		Wild-type strain
Genetic reagent (<i>Danio rerio</i>)	<i>Tg(mpx:EGFP)¹¹⁴</i>	Uni of Sheffield PMID: 16926288	ZFIN ID: ZDB-ALT-070118-2	
Genetic reagent (<i>Danio rerio</i>)	<i>Tg(fli1:EGFP)^{y1}</i>	ZIRC PMID: 16671106	ZFIN ID: ZDB-ALT-011017-8	
Genetic reagent (<i>Danio rerio</i>)	<i>hai1a^{fr26}</i>	Hammerschmidt lab; Max Planck Freiburg PMID: 31819976	ZFIN ID: ZDB-ALT-200618-2	= <i>spint1a^{fr26}</i>
Genetic reagent (<i>Danio rerio</i>)	<i>hai1a^{hi2217}</i>	Nancy Hopkins lab; Massachusetts Institute of Technology PMID: 17728346	ZFIN ID: ZDB-ALT-040924-4	= <i>spint1a^{hi2217Tg}</i>
Genetic reagent (<i>Danio rerio</i>)	<i>ddi^{ti251}</i>	Nuesslein-Volhard lab; Max Planck Tuebingen PMID: 9007245	ZFIN ID: ZDB-ALT-980203-1462	= <i>dandruff spint1a^{ti251}</i> = <i>hai1a^{ti251}</i>
Genetic reagent (<i>Danio rerio</i>)	<i>ddi^{ti419}</i>	Nuesslein-Volhard lab; Max Planck Tuebingen PMID: 9007245		= <i>dandruff spint1a^{ti419}</i> = <i>hai1a^{ti419}</i>
Genetic reagent (<i>Danio rerio</i>)	<i>st14a^{sq10}</i>	Our lab PMID: 31645615	ZFIN ID: ZDB-ALT-200219-5	
Genetic reagent (<i>Danio rerio</i>)	<i>Tg(6xNfkb:EGFP)^{nc1}</i>	Rawls lab PMID: 21439961	ZFIN ID: ZDB-ALT-120409-6	

Continued on next page

Continued

Reagent type (species) or resource	Designation	Source or reference	Identifiers	Additional information
Genetic reagent (<i>Danio rerio</i>)	<i>Tg(krtt1c19e:LY-Tomato)^{sq16}</i>	Our lab. Lee et al: PMID: 24400120	ZFIN ID: ZDB-ALT-140424-2	
Genetic reagent (<i>Danio rerio</i>)	<i>Tg(actb2:GCaMP6s, myl7:mCherry)^{kcc2}</i>	This paper		Plasmid from Solnica-Krezel Lab. Injected with Tol2 RNA to make line
Antibody	Chicken anti-eGFP antibody	Abcam	ab13970, RRID: AB_300798	1:500
Antibody	Rabbit anti-eGFP	Torrey Pines Biolabs	Tp401 RRID: AB_10013661	1:500
Antibody	Rabbit anti-FITC	Thermo Fisher Scientific	71-1900 RRID: AB_2533978	1:200
Antibody	Rabbit anti-p90RSK (Phospho-Thr ³⁴⁸)	GenScript	A00487	1:100
Antibody	Rabbit anti-beta catenin	Abcam	ab6302 RRID: AB_305407	1:200
Antibody	Mouse anti-E-cadherin	BD Biosciences	610181 RRID: AB_397580	1:200
Antibody	Mouse anti-Tp63	Biocare Medical	CM163 RRID: AB_10582730	1:200
Antibody	Rabbit anti-phospho-p44/42 MAPK (Erk1/2) (Thr ²⁰² /Tyr ²⁰⁴)	Cell Signaling Technology	Cat# 4370, RRID: AB_2315112	1:100
Antibody	Rabbit anti-p44/42 MAPK (Erk1/2)	Cell Signaling Technology	Cat# 9102, RRID: AB_330744	1:100
Antibody	Alexa Fluor-488 Donkey anti-rabbit	Life Technologies	A21206 RRID: AB_2535792	1:700
Antibody	Alexa Fluor-647 Donkey anti-rabbit	Life Technologies	A31573 RRID: AB_253618	1:700
Antibody	Alexa Fluor-546 Donkey anti-mouse	Life Technologies	A10036 RRID: AB_2534012	1:700
Antibody	Alexa Fluor-488 Goat anti-chicken	Life Technologies	A11039 RRID: AB_2534096	1:700
Recombinant DNA reagent	pCS2+-PKCδ-GFP	Amaya Lab, Uni of Manchester PMID: 15866160		For making <i>PKCδ-GFP</i> RNA
Recombinant DNA reagent	pT3Ts-Tol2	Ekker Lab, Mayo Clinic PMID: 17096595	Addgene Plasmid #31831 RRID: Addgene_31831	
Recombinant DNA reagent	pCS2+-GCaMP6s	Solnica-Krezel Lab, Washington University School of Medicine, St. Louis, MO		For making <i>GCaMP6s</i> RNA
Recombinant DNA reagent	<i>p(actb2:GCaMP6s, myl7:mCherry)</i>	Solnica-Krezel Lab, Washington University School of Medicine, St. Louis, MO. PMID: 28322738		For making stable transgenic line
Sequence-based reagent	<i>duox</i> morpholino	GeneTools	PMID: 19494811	5' AGTGAATTAGAGAAA TGACCTTTT 3' (0.4 mM)
Sequence-based reagent	<i>p53</i> morpholino	GeneTools	PMID: 19494811	5' GCGCCATTGCTTTGCA AGAATTG 3' (0.2 mM)
Sequence-based reagent	Oligo(dT)12–18 Primer	Invitrogen	PMID: 18418012	
Sequence-based reagent	<i>nfkbiaa</i>	This paper	PCR primers	F-5' AGACGCAAAGGAGC AGTG TAG 3' R- 5' TGTGTGTCTGCCGA AGGTC 3'

Continued on next page

Continued

Reagent type (species) or resource	Designation	Source or reference	Identifiers	Additional information
Sequence-based reagent	<i>eef1a11</i>	This paper	PCR primers	F'-5' CTGGAGGCCAGC TCAAACAT 3' R-5' ATCAAGAAGAGTAGT ACCGCTAGCATTAC 3'
Sequence-based reagent	<i>rps6ka3a</i> in situ probe	This paper	PCR primers for cloning probe	F'-5' ATACTCCAGTCCC ACCGGA 3' R- 5'TGGTGATGATGGT AGACTCGC 3'
Peptide, recombinant protein	Proteinase K	Thermo Scientific	EO0491	0.5 µg/µl
Commercial assay or kit	SuperScript III Reverse Transcriptase	Invitrogen	18080093	
Commercial assay or kit	TRIzol Reagent	Invitrogen	15596026	
Commercial assay or kit	GoTaq G2 Green Master Mix	Promega	M7823	Functions used: TrackMate Reslice Average Intensity
Commercial assay or kit	iTaq Universal SYBR Green Supermix	Bio-Rad	1725121	Functions used: Spot
Commercial assay or kit	mMESSAGE mMACHINE SP6 Transcription Kit	Invitrogen	AM1340	Tests: Student's t-test, Chi-squared test, Mann-Whitney test, ANOVA with Bonferroni or Dunn's post-tests
Commercial assay or kit	mMESSAGE mMACHINE T3 Transcription Kit	Invitrogen	AM1348	
Commercial assay or kit	MEGAscript T7 Transcription Kit	Invitrogen	AM1350	
Commercial assay or kit	pGEM-T Easy	Promega	A137A	
Commercial assay or kit	pCR 2.1-TOPO TA vector	Invitrogen	K450040	
Commercial assay or kit	QIAquick PCR Purification Kit	Qiagen	28104	
Commercial assay or kit	DIG RNA Labeling Kit	Roche	11175025910	
Commercial assay or kit	SP6 RNA Polymerase	Roche	10 810 274 001	
Commercial assay or kit	NBT/BCIP Stock Solution	Roche	11681451001	
Chemical compound, drug	Diphenyleneiodonium chloride	Sigma-Aldrich	D2926	40 µM
Chemical compound, drug	Thapsigargin	Sigma-Aldrich	T9033	6.25 µM
Chemical compound, drug	Bisindolylmaleimide I (GF109203X)	Selleckchem	S7208	85 µM
Chemical compound, drug	YM-254890	FocusBiomolecules	10-1590-0100	32 µM
Chemical compound, drug	2-Aminoethyl diphenylborinate	Sigma-Aldrich	D9754	2.5 µM
Chemical compound, drug	BI-D1870	Axon Medchem	Axon-1528	1.2 µM

Continued on next page

Continued

Reagent type (species) or resource	Designation	Source or reference	Identifiers	Additional information
Chemical compound, drug	Dimethyl fumarate	Sigma-Aldrich	242926	9 μ M
Chemical compound, drug	Phorbol 12-myristate 13-acetate	Sigma-Aldrich	P8139	37.5 or 125 ng/ml
Chemical compound, drug	U0126	Cell Signaling Technology	9903	100 μ M
Chemical compound, drug	PD184352 (CI-1040)	Selleckchem	S1020	1.3 μ M
Chemical compound, drug	DAPI (4',6-diamidino-2-phenylindole, dihydrochloride)	Invitrogen	D1306	5 μ g/ml
Chemical compound, drug	Penta-fluorobenzenesulfonyl fluorescein	Cayman Chemicals	10005983	12.5 μ M
Chemical compound, drug	Fluorescein isothiocyanate–dextran	Sigma-Aldrich	FD4	2.5 mg/ml
Software, algorithm	Fiji (ImageJ 1.52p)	NIH	https://imagej.nih.gov/	Functions used: TrackMate Reslice Average Intensity
Software, algorithm	Imaris 9.6.0	Oxford Instruments		Functions used: Spot
Software, algorithm	Prism 9.1.1	GraphPad		Tests: Student's t-test, Chi-squared test, Mann–Whitney test, ANOVA with Bonferroni or Dunn's post-tests
Software, algorithm	Photoshop 22.1.1 release	Adobe		

Zebrafish husbandry and lines

Fish were housed at the IMCB and the NTU zebrafish facilities under IACUC numbers #140924 and #A18002, respectively, and according to the guidelines of the National Advisory Committee for Laboratory Animal Research. Embryos were derived by natural crosses and staged as per *Kimmel et al., 1995* and raised in 0.5 \times E2 medium (7.5 mM NaCl, 0.25 mM KCl, 0.5 mM MgSO₄, 75 μ M KH₂PO₄, 25 μ M Na₂HPO₄, 0.5 M CaCl₂, 0.35 mM NaHCO₃). Anaesthesia was administered in E2 medium (embryos) or fish tank water (adults) using 0.02% pH 7.0 buffered Tricaine MS-222 (Sigma). The *hai1a/ddf* alleles used were *hai1a*^{hi2217}, *hai1a*^{fr26}, *ddf*^{ti251}, and *ddf*^{ti419}. The *st14a*^{sq10} allele was generated previously (*Lin et al., 2019*). For imaging neutrophils and keratinocytes, the transgenic lines *Tg(mpx:EGFP)*ⁱ¹¹⁴ (*Renshaw et al., 2006*) and *Tg(krtt1c19e:lyn-tdtomato)*^{sq16} (*Lee et al., 2014*) were used, whilst early leukocytes were imaged with *Tg(fli1:EGFP)*^{y1} (*Redd et al., 2006*). To image Nf κ B pathway activity, the *Tg(6xHsa.NFKB:EGFP)*^{nc1} sensor line was used (*Kanther et al., 2011*). Calcium imaging was performed by injection of *GCaMP6s* RNA (see below) or using a *Tg(actb2:GCaMP6s, myl7:mCherry)*^{kc2} stable transgenic line, generated via plasmid (*Chen et al., 2017*) and *Tol2* RNA co-injection.

Genomic DNA and RNA extraction, reverse transcription, and PCR

Adult fin clips or embryos were isolated following anaesthesia, and genomic DNA extracted by incubation at 55°C for 4 hr in Lysis buffer (10 mM Tris pH 8.3, 50 mM KCl, 0.3% Tween20, 0.3% Nonidet P-40, 0.5 μ g/ μ l Proteinase K). PCRs were performed using GoTaq (Promega) on a Veriti thermal cycler (Applied Biosystems) and purified with a PCR purification kit (Qiagen). TRIzol (Invitrogen) was used for RNA extraction following provided protocol, and cDNA generated from 1 μ g total RNA

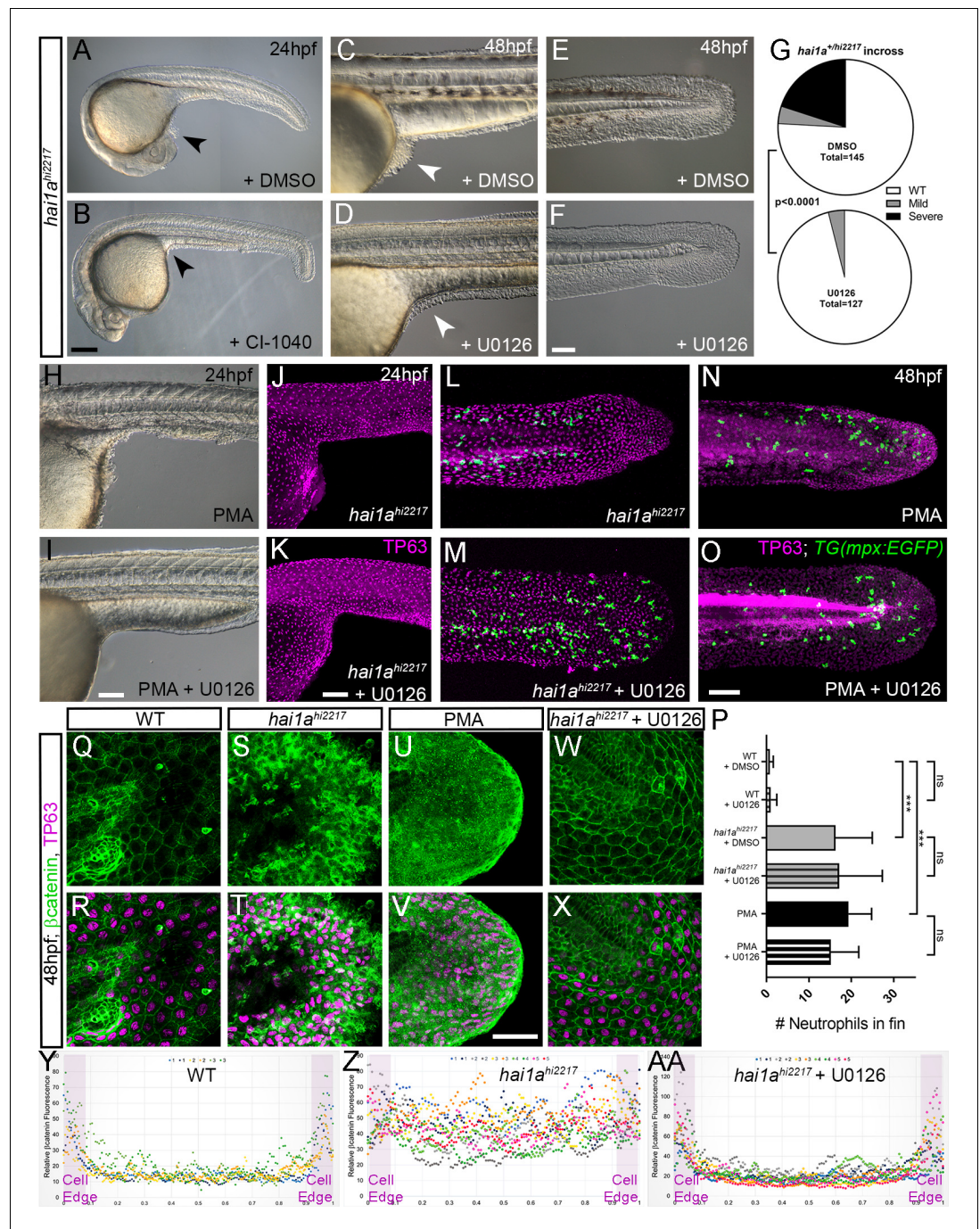


Figure 9. Rescue of the *hai1a* epidermal phenotype by pERK inhibitors. (A–F) Lateral DIC images of 24hpf (A, B) or 48hpf (C–F) *hai1a*^{hi2217} embryos treated with either DMSO (A, C, E), 1.3 μM CI-1040 (B), or 100 μM U0126 (D, F) showing rescue of general morphology (B), trunk (D), and tail (F) epidermal phenotypes compared to DMSO-treated *hai1a*^{hi2217}. Epidermal aggregates under the yolk are reduced in the treated mutants (A–D; arrowheads). (G) Proportion of 48hpf larvae derived from *hai1a*^{+/hi2217} incross showing mild or severe *hai1a* epidermal phenotype following DMSO (upper) or U0126 (lower) treatment (Chi-squared test). (H, I) Lateral DIC images of 24hpf embryo treated with 125 ng/ml phorbol 12-myristate 13-acetate (PMA) (H) or PMA and U0126 (I). Yolk-associated epidermal aggregates are reduced. (J–M) Lateral projected confocal images of *hai1a*^{hi2217}; *Tg(mpx:eGFP)*¹¹⁴ trunk at 24hpf (J, K) and tail at 48hpf (L, M), either treated with 0.5% DMSO (J, L) or U0126 (K, M). Embryos are immunostained for TP63 (magenta) and eGFP (green), highlighting rescue of epidermal phenotype but no reduction of neutrophils. (N, O) Lateral projected confocal images of *Tg(mpx:eGFP)*¹¹⁴ treated with PMA alone (N) or PMA with U0126 (O) and immunostained for TP63 (magenta) and eGFP (green). Fin morphology is

Figure 9 continued on next page

Figure 9 continued

restored but neutrophils are still present. (P) Quantification of neutrophils in the fins showing U0126 does not reduce inflammation induced by loss of *hai1a* or PMA treatment. $n = 8$; ANOVA with Bonferroni post-test; $***p < 0.001$. (Q–X) Projected confocal images of 48hpf larval tails immunostained for β -catenin (green) and TP63 (magenta; R, T, V, X) of WT (Q, R, U, V) and *hai1a*^{hi2217} (S, T, W, X), either untreated (Q–T), treated with PMA (U, V) or U0126 (W, X). (Y–AA) Profile plots of fluorescence distribution across cells of WT (Y), *hai1a*^{hi2217} (Z), and *hai1a*^{hi2217} treated with U0126 (AA). X-axis represents width of the cell. β -catenin immunofluorescence intensity (Y-axis) shows majority at cell edge (demarcated in light purple) in WT and rescued *hai1a* mutants, but is distributed in cytoplasm in mutant. Two cells per 3–5 larvae were analysed. Scale bars: (B) = 200 μ m, (F, I, K, O) = 100 μ m, (V) = 20 μ m.

The online version of this article includes the following figure supplement(s) for figure 9:

Figure supplement 1. Rescue of the *hai1a* epidermal phenotype by pERK inhibitors.

Figure supplement 2. The barrier function of the *hai1a* epidermis is not grossly compromised.

using SuperScript III Reverse Transcriptase (Invitrogen) with Oligo(dT)12-18 primer. For qPCR, iTaq SYBR green (Bio-Rad) was used to amplify, with reaction dynamics measured on a Bio-Rad CFX96 Real-Time PCR Detection System. For measuring *nfkbiaa* mRNA by qPCR, the following primers (5' to 3') were used to amplify a region encoded on exons 4 and 5: F-AGACGCAAAGGAGCAGTGTAG, R-TGTGTGTCTGCCAAGGTC. Reference gene was *eef1a111* and the primers used amplified between exon 3 to 4: F-CTGGAGGCCAGCTCAAACAT, R- ATCAAGAAGAGTAGTACCGCTAGCA TTAC.

RNA synthesis

RNAs for *GCaMP6s* and *PKC δ -GFP* were synthesised from pCS2-based plasmids containing the respective coding sequences (Sivak et al., 2005; Chen et al., 2017). These were linearised with *NotI* (NEB), and RNA in vitro transcribed with mMESSAGE mMACHINE SP6 Transcription Kit (Ambion). RNA for *Tol2* was generated from the pT3Ts-Tol2 plasmid, linearised with *SmaI* (NEB), and transcribed with the mMESSAGE mMACHINE T3 Transcription Kit (Ambion). RNA for injection was purified by lithium chloride precipitation.

Embryo injection and morpholino

Embryos were aligned on an agarose plate and injected at the one-cell stage with RNA or morpholino diluted in Phenol Red and Danieau's buffer using a PLI-100 microinjector (Harvard Apparatus). Injection needles were pulled from borosilicate glass capillaries (0.5 mm inner diameter, Sutter) on a Sutter P-97 micropipette puller. The Duox morpholino (AGTGAATTAGAGAAATGCACCTTTT) was purchased from GeneTools and injected at 0.4 mM with 0.2 mM of the tp53 morpholino (GCGCCA TTGCTTTGCAAGAATTG).

TALEN mutagenesis

To generate the *ikbkg* mutant, TALEN vectors targeting the sequence ATGGAGGGCTGG in second exon were designed and constructed by ToolGen (<http://toolgen.com>). TALEN vectors were linearised with *PvuII* (NEB) and purified using a PCR purification kit (Qiagen), and then used for in vitro transcription with the MEGAscript T7 kit (Ambion). About 170–300 pg of supplied ZFN RNAs or purified TALEN RNAs were then injected into one-cell stage WT zebrafish embryos, which were raised to 24 hr, then genomic DNA extracted.

For detection of fish with edited loci, PCR was performed on genomic DNA of injected fish with primers flanking the target site, cloned by TA cloning into pGEMT-Easy (Promega) or pCR2.1-TOPO-TA (Invitrogen) and individual clones sequenced to establish efficiency. Other embryos were raised to adulthood and their offspring were similarly genotyped to identify founder mutants.

Small-molecule treatment

All compounds for treating embryos were dissolved in DMSO, diluted in 0.5 \times E2 Embryo Medium and embryos treated by immersion. The compounds, and concentrations used, with catalogue numbers were diphenyleneiodonium chloride (DPI), 40 μ M (D2926, Sigma); thapsigargin, 6.25 μ M (T9033, Sigma); bisindolylmaleimide I (GF109203X), 85 μ M (S7208, Selleckchem); YM-254890, 32 μ M

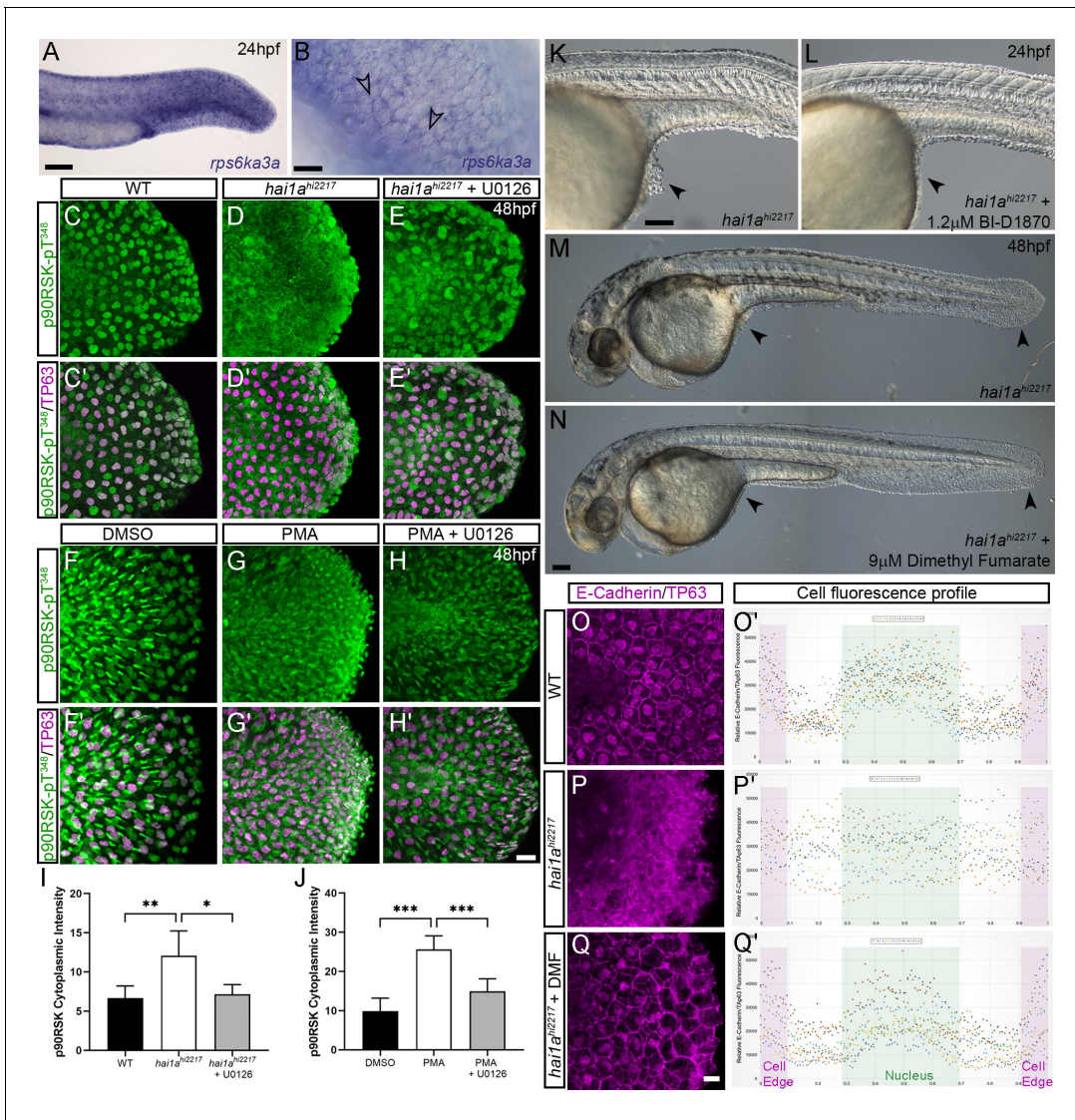


Figure 10. Altered RSK status in *hai1a*^{hi2217} accounts for epidermal defects. (A, B) In situ hybridisation of *rps6ka3a* at 24hpf under low- (A) and high-power (B) magnification showing expression in basal keratinocytes. Open arrowheads in (B) indicate borders of EVL cells bisecting nuclei of underlying *rps6ka3a*-positive cells. (C–H') Lateral projected confocal images of the tails of embryos immunostained for p90RSK (Phospho-Thr³⁴⁸) (C–H') and TP63 (C'–H'). In both the *hai1a*^{hi2217} (D, D') and 125 ng/ml phorbol 12-myristate 13-acetate (PMA)-treated (G, G') embryos, there is an increase in cytoplasmic levels of p90RSK (Phospho-Thr³⁴⁸) signal above the nuclear only signal seen in WT (C, C') or DMSO (F, F'). Treatment with the pERK inhibitor U0126 reduced cytoplasmic levels but did not affect nuclear signal (E, E'; H, H'). (I, J) Quantification of immunofluorescent intensity of cytoplasmic levels of p90RSK (Phospho-Thr³⁴⁸) in basal keratinocytes of tails of 48hpf WT and *hai1a*^{hi2217}, treated with DMSO or U0126 (I), and PMA or PMA plus U0126 (J). Nucleus signal was excluded by masking from the DAPI channel. n = 5; t-test; ***p<0.001, **p<0.01, *p<0.05. (K–N) Lateral DIC images of *hai1a*^{hi2217} embryos at 24hpf (K, L) and 48hpf (M, N) untreated (K, M) or treated with 1.2 μM BI-D1870 (L) or 9 μM dimethyl fumarate (DMF). Locations of epidermal aggregates and loss of tail fin morphology in *hai1a* mutants, and their rescue by RSK inhibitor treatment are indicated by arrowheads. (O–Q) Lateral projected confocal images of the tails of embryos immunostained with antibodies against E-cadherin and TP63 in WT (O, P) and *hai1a*^{hi2217} treated with DMF (Q). (O'–Q') Profile plots of fluorescence distribution across cells of WT (O), *hai1a*^{hi2217} (P), and *hai1a*^{hi2217} treated with DMF (Q'). X-axis represents width of the cell. β-Catenin immunofluorescence intensity (Y-axis) shows majority at cell edge (E-cadherin domain demarcated in light purple) and centre of cell (nucleus demarcated in light green) in WT and rescued *hai1a* mutants, but there is no clear membrane signal in the untreated *hai1a* mutants. Two cells per five larvae were analysed. Scale bars: (A, K, N) = 100 μm; (B, H) p=20 μm.

The online version of this article includes the following figure supplement(s) for figure 10:

Figure supplement 1. RSK inhibitors rescue the *hai1a* phenotype.

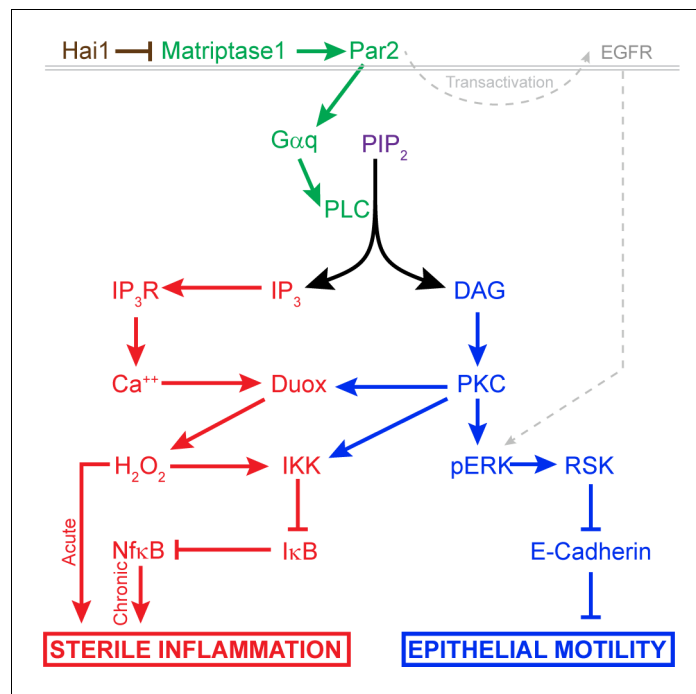


Figure 11. Model of pathway-activated downstream of Hai1 and Matriptase. Proposed model of pathways downstream of Hai1 which drives chronic and acute sterile inflammation (red) and epithelial motility (blue). A previously defined transactivation of EGFR is also integrated. Other pathways known to act downstream of Matriptase, involving cMet, PI3K, AKT, and mTOR, are not shown.

(10-1590-0100, Focus Biomolecules); 2-aminoethyl diphenylborinate (2-APB), 2.5 μ M (D9754, Sigma), BI-D1870, 1.2 μ M (Axon-1528, Axon Medchem); dimethyl fumarate, 9 μ M (242926, Sigma); phorbol 12-myristate 13-acetate (PMA), 37.5 or 125 ng/ml (P8139, Sigma); U0126, 100 μ M (9903, Cell Signaling Technology); PD184352 (CI-1040), 1.3 μ M (S1020, Selleckchem). Unless otherwise stated, controls for all experiments were exposed to 0.5% DMSO carrier in 0.5 \times E2 Embryo Medium.

Proteomic analysis

Batches of 100 WT, *ddf⁴¹⁹*, and *ddf^{ti251}* embryos were collected at 24 hr and 48 hr, dechorionated, deyolked, and protein extracted as per *Alli Shaik et al., 2014*. Protein was precipitated in 100% methanol at 4°C, then resuspended in 2-D cell lysis buffer (30 mM Tris-HCl, pH 8.8, containing 7 M urea, 2 M thiourea, and 4% CHAPS). 2-D DIGE and mass spectrometry protein identification was performed by Applied Biomics (Hayward, CA). Protein samples were labelled with either Cy2, Cy3, or Cy5, mixed, and then subjected to 2-D DIGE to separate individual proteins. Gels were scanned using Typhoon TRIO (Amersham BioSciences) and analysed by Image QuantTL and DeCyder (ver. 6.5) software (GE-Healthcare). Spots with more than 1.5-fold change were picked, in-gel trypsin digested, and protein identification performed by MALDI-TOF mass spectrometry and MASCOT search engine in the GPS Explorer software (Matrix Science).

In situ hybridisation

A probe corresponding to the final 1078 bp of *rps6ka3a* (*RSK2a*; NM_212786.1) was generated by cloning a PCR-derived cDNA fragment into in pGEMT-Easy (Promega), linearising with *ApaI* (NEB) and transcribing a DIG probe with SP6 RNA polymerase (Roche). Whole-mount in situ hybridisation developed with NBT/BCIP (Roche) was performed as described (*Thisse and Thisse, 2008*).

Immunofluorescent, dye staining, and TUNEL

For antibody staining, embryos were fixed in 4% paraformaldehyde overnight at 4°C and then washed in PBT (0.1% Triton in PBS), permeabilised in -20°C acetone for 7 min, washed in PBT,

blocked for 3 hr in Block solution (PBT supplemented with 4% BSA and 1% DMSO), then incubated overnight at 4°C with primary antibody diluted in Block solution, washed extensively in PBT, re-blocked in Block solution, then incubated overnight at 4°C with fluorescent secondary antibody diluted in Block solution. Following extensive PBT washing, embryos were cleared in 80% glycerol/PBS before imaging. Primary antibodies used and their dilutions are as follows: Chicken anti-eGFP antibody, 1:500 (ab13970, Abcam), Rabbit anti-eGFP, 1:500 (Tp401, Torrey Pines Biolabs), Rabbit anti-FITC, 1:200 (#71-1900, Thermo Fisher), Rabbit anti-beta catenin, 1:200 (ab6302, Abcam), Mouse anti-E-cadherin, 1:200 (#610181, BD Biosciences), Mouse anti-Tp63, 1:200 (CM163, Biocare Medical), Rabbit anti-phospho-p44/42 MAPK (Erk1/2) (Thr²⁰²/Tyr²⁰⁴), 1:100 (#4370, Cell Signaling Technology), Rabbit anti-p44/42 MAPK (Erk1/2), 1:100 (#9102, Cell Signaling Technology), and Rabbit anti-p90RSK (Phospho-Thr³⁴⁸), 1:100 (A00487, GenScript). All secondary antibodies were purchased from Invitrogen and used at 1:700 and were Alexa Fluor-488 Donkey anti-rabbit (A21206), Alexa Fluor-647 Donkey anti-rabbit (A31573), Alexa Fluor-546 Donkey anti-mouse (A10036), and Alexa Fluor-488 Goat anti-chicken (A-11039). Nuclei were counterstained using 5 µg/ml of DAPI (4',6-diamidino-2-phenylindole, dihydrochloride; D1306, Invitrogen) added during secondary antibody incubation.

To stain hydrogen peroxide, embryos were incubated for 60 min at room temperature with 12.5 µM PFBSF (#10005983, Cayman Chemicals), then rinsed in Embryo Medium, anaesthetised, and imaged.

Fluorescent TUNEL staining was performed using the Fluorescein In Situ Cell Death Detection Kit (11684795910, Roche), with the fluorescein detected by antibody staining using rabbit anti-FITC, and co-immunostained for TP63 and eGFP. Epidermal permeability assays were conducted by immersing 36hpf embryos in 2.5 mg/ml fluorescein isothiocyanate-dextran 3–5 kDa (Sigma) or 0.075% methylene blue for 30 min and then destained in E2 medium.

Microscopy and statistical analysis

Still and timelapse imaging was performed on upright Zeiss Axiolmager M2, Zeiss Light-sheet Z.1, upright Zeiss LSM800 Confocal Microscope or Zeiss AxioZoom V16 microscopes. Embryos were mounted in 1.2% Low Melting Point Agarose (Mo Bio Laboratories) in 0.5× E2 medium in 35 mm glass-bottom imaging dishes (MatTek) or in a 1 mm inner diameter capillary for light-sheet time-lapse. When imaging was performed on live embryos, the embryo media were supplemented with buffered 0.02% Tricaine and imaging conducted at 25°C. Image processing was done using Zen 3.1 software (Zeiss), Fiji (ImageJ, ver. 1.52p), or Imaris (Bitplane) and compiled using Photoshop 2020 (Adobe). Neutrophils were tracked with TrackMate in Fiji or using the Spot function in Imaris. Kymographs were generated using the Reslice function in Fiji following generation of a line of interest across image. Fluorescence intensities were calculated using the Average Intensity function in Fiji following generation of a Region of Interest and masking of the DAPI channel to exclude the nucleus when required. In statistical analyses, n = number of embryos or cells measured, and as defined in the figure legend. GraphPad Prism was used for statistical analyses and graph generation. In all statistical tests, *p<0.05, **p<0.01, ***p<0.001. Tests used are indicated in the associated figure legend and were Student's t-test, Chi-squared test, Mann–Whitney test, or ANOVA with Bonferroni or Dunn's post-tests.

Additional information

Funding

Funder	Grant reference number	Author
Ministry of Education - Singapore	2015-T1-001-035	Jiajia Ma Tom J Carney
Ministry of Education - Singapore	MOE2016-T3-1-005	Harsha Mahabaleshwar

The funders had no role in study design, data collection and interpretation, or the decision to submit the work for publication.

Author contributions

Jiajia Ma, Formal analysis, Investigation, Writing - original draft; Claire A Scott, Ying Na Ho, Ser Sue Ng, Formal analysis, Investigation; Harsha Mahabaleshwar, Data curation, Formal analysis; Katherine S Marsay, Changqing Zhang, Christopher KJ Teow, Investigation; Weibin Zhang, Resources; Vinay Tergaonkar, Sudipto Roy, Resources, Supervision; Lynda J Partridge, Enrique Amaya, Supervision; Tom J Carney, Conceptualization, Formal analysis, Supervision, Funding acquisition, Investigation, Writing - original draft, Project administration

Author ORCIDs

Tom J Carney  <https://orcid.org/0000-0003-2371-1924>

Ethics

Animal experimentation: Fish were housed at the IMCB and the NTU zebrafish facilities under IACUC numbers #140924 and #A18002 respectively, and according to the guidelines of the National Advisory Committee for Laboratory Animal Research. Approval was provided by the Institutional Animal Care and Use Committees of the Biological Resource Centre (IMCB) and NTU according to Agri-Food and Veterinary Authority (AVA) Rules and the National Advisory Committee for Laboratory Animal Research (NACLAR) requirements.

Decision letter and Author response

Decision letter <https://doi.org/10.7554/eLife.66596.sa1>

Author response <https://doi.org/10.7554/eLife.66596.sa2>

Additional files

Supplementary files

- Transparent reporting form

Data availability

All data generated or analysed during this study are included in the manuscript and supporting files.

References

- Al-Ani B, Hewett PW, Cudmore MJ, Fujisawa T, Saifeddine M, Williams H, Ramma W, Sissaoui S, Jayaraman PS, Ohba M, Ahmad S, Hollenberg MD, Ahmed A. 2010. Activation of proteinase-activated receptor 2 stimulates soluble vascular endothelial growth factor receptor 1 release via epidermal growth factor receptor transactivation in endothelial cells. *Hypertension* **55**:689–697. DOI: <https://doi.org/10.1161/HYPERTENSIONAHA.109.136333>, PMID: 20124108
- Allen LF, Sebolt-Leopold J, Meyer MB. 2003. CI-1040 (PD184352), a targeted signal transduction inhibitor of MEK (MAPKK). *Seminars in Oncology* **30**:105–116. DOI: <https://doi.org/10.1053/j.seminoncol.2003.08.012>, PMID: 14613031
- Alli Shaik A, Wee S, Li RH, Li Z, Carney TJ, Mathavan S, Gunaratne J. 2014. Functional mapping of the zebrafish early embryo proteome and transcriptome. *Journal of Proteome Research* **13**:5536–5550. DOI: <https://doi.org/10.1021/pr5005136>, PMID: 25230361
- Anastasaki C, Rauen KA, Patton EE. 2012. Continual low-level MEK inhibition ameliorates cardio-facio-cutaneous phenotypes in zebrafish. *Disease Models & Mechanisms* **5**:546–552. DOI: <https://doi.org/10.1242/dmm.008672>, PMID: 22301711
- Andersen JL, Gesser B, Funder ED, Nielsen CJF, Gotfred-Rasmussen H, Rasmussen MK, Toth R, Gothelf KV, Arthur JSC, Iversen L, Nissen P. 2018. Dimethyl fumarate is an allosteric covalent inhibitor of the p90 ribosomal S6 kinases. *Nature Communications* **9**:4344. DOI: <https://doi.org/10.1038/s41467-018-06787-w>, PMID: 30341347
- Armistead J, Hatzold J, van Roye A, Fahle E, Hammerschmidt M. 2020. Entosis and apical cell extrusion constitute a tumor-suppressive mechanism downstream of matriptase. *Journal of Cell Biology* **219**:e201905190. DOI: <https://doi.org/10.1083/jcb.201905190>
- Böhm SK, Khitin LM, Grady EF, Aponte G, Payan DG, Bunnett NW. 1996. Mechanisms of desensitization and resensitization of proteinase-activated receptor-2. *Journal of Biological Chemistry* **271**:22003–22016. DOI: <https://doi.org/10.1074/jbc.271.36.22003>, PMID: 8703006

- Carney TJ**, von der Hardt S, Sonntag C, Amsterdam A, Topczewski J, Hopkins N, Hammerschmidt M. 2007. Inactivation of serine protease Matriptase1a by its inhibitor Hai1 is required for epithelial integrity of the zebrafish epidermis. *Development* **134**:3461–3471. DOI: <https://doi.org/10.1242/dev.004556>, PMID: 17728346
- Čáslavský J**, Klímová Z, Vomastek T. 2013. ERK and RSK regulate distinct steps of a cellular program that induces transition from multicellular epithelium to single cell phenotype. *Cellular Signalling* **25**:2743–2751. DOI: <https://doi.org/10.1016/j.cellsig.2013.08.024>, PMID: 24012955
- Chen J**, Xia L, Bruchas MR, Solnica-Krezel L. 2017. Imaging early embryonic calcium activity with GCaMP6s transgenic zebrafish. *Developmental Biology* **430**:385–396. DOI: <https://doi.org/10.1016/j.ydbio.2017.03.010>, PMID: 28322738
- Chou CM**, Chen YC, Su S, Chen GD, Huang KY, Lien HW, Huang CJ, Cheng CH. 2015. Activation of MEK2 is sufficient to induce skin papilloma formation in transgenic zebrafish. *Journal of Biomedical Science* **22**:102. DOI: <https://doi.org/10.1186/s12929-015-0207-2>, PMID: 26572230
- Chuderland D**, Marmor G, Shainskaya A, Seger R. 2020. Calcium-Mediated interactions regulate the subcellular localization of extracellular Signal-Regulated kinases (ERKs). *Cellular Physiology and Biochemistry : International Journal of Experimental Cellular Physiology, Biochemistry, and Pharmacology* **54**:474–492. DOI: <https://doi.org/10.33594/000000231>, PMID: 32392404
- Chung H**, Ramachandran R, Hollenberg MD, Muruve DA. 2013. Proteinase-activated receptor-2 transactivation of epidermal growth factor receptor and transforming growth factor- β receptor signaling pathways contributes to renal fibrosis. *Journal of Biological Chemistry* **288**:37319–37331. DOI: <https://doi.org/10.1074/jbc.M113.492793>, PMID: 24253040
- Darmoul D**, Gratio V, Devaud H, Laburthe M. 2004. Protease-activated receptor 2 in Colon cancer: trypsin-induced MAPK phosphorylation and cell proliferation are mediated by epidermal growth factor receptor transactivation. *The Journal of Biological Chemistry* **279**:20927–20934. DOI: <https://doi.org/10.1074/jbc.M401430200>, PMID: 15010475
- de Oliveira S**, López-Muñoz A, Candel S, Pelegrín P, Calado Â, Mulero V. 2014. ATP modulates acute inflammation in vivo through dual oxidase 1-derived H₂O₂ production and NF- κ B activation. *Journal of Immunology* **192**:5710–5719. DOI: <https://doi.org/10.4049/jimmunol.1302902>, PMID: 24842759
- Enyedi B**, Niethammer P. 2015. Mechanisms of epithelial wound detection. *Trends in Cell Biology* **25**:398–407. DOI: <https://doi.org/10.1016/j.tcb.2015.02.007>, PMID: 25813429
- Favata MF**, Horiuchi KY, Manos EJ, Daulerio AJ, Stradley DA, Feeser WS, Van Dyk DE, Pitts WJ, Earl RA, Hobbs F, Copeland RA, Magolda RL, Scherle PA, Trzaskos JM. 1998. Identification of a novel inhibitor of mitogen-activated protein kinase kinase. *Journal of Biological Chemistry* **273**:18623–18632. DOI: <https://doi.org/10.1074/jbc.273.29.18623>, PMID: 9660836
- Feng Y**, Santoriello C, Mione M, Hurlstone A, Martin P. 2010. Live imaging of innate immune cell sensing of transformed cells in zebrafish larvae: parallels between tumor initiation and wound inflammation. *PLOS Biology* **8**:e1000562. DOI: <https://doi.org/10.1371/journal.pbio.1000562>, PMID: 21179501
- Gault WJ**, Enyedi B, Niethammer P. 2014. Osmotic surveillance mediates rapid wound closure through nucleotide release. *Journal of Cell Biology* **207**:767–782. DOI: <https://doi.org/10.1083/jcb.201408049>, PMID: 25533845
- Gawecka JE**, Young-Robbins SS, Sulzmaier FJ, Caliva MJ, Heikkilä MM, Matter ML, Ramos JW. 2012. RSK2 protein suppresses integrin activation and fibronectin matrix assembly and promotes cell migration. *Journal of Biological Chemistry* **287**:43424–43437. DOI: <https://doi.org/10.1074/jbc.M112.423046>, PMID: 23118220
- Goon Goh F**, Sloss CM, Cunningham MR, Nilsson M, Cadalbert L, Plevin R. 2008. G-protein-dependent and -independent pathways regulate proteinase-activated receptor-2 mediated p65 NF κ B serine 536 phosphorylation in human keratinocytes. *Cellular Signalling* **20**:1267–1274. DOI: <https://doi.org/10.1016/j.cellsig.2008.02.015>, PMID: 18424071
- Hatzold J**, Beleggia F, Herzig H, Altmüller J, Nürnberg P, Bloch W, Wollnik B, Hammerschmidt M. 2016. Tumor suppression in basal keratinocytes via dual non-cell-autonomous functions of a Na,K-ATPase beta subunit. *eLife* **5**:e14277. DOI: <https://doi.org/10.7554/eLife.14277>, PMID: 27240166
- Jiang X**, Bailly MA, Panetti TS, Cappello M, Konigsberg WH, Bromberg ME. 2004. Formation of tissue factor-factor VIIa-factor xa complex promotes cellular signaling and migration of human breast Cancer cells. *Journal of Thrombosis and Haemostasis* **2**:93–101. DOI: <https://doi.org/10.1111/j.1538-7836.2004.00545.x>, PMID: 14717972
- Kang S**, Elf S, Lythgoe K, Hitosugi T, Taunton J, Zhou W, Xiong L, Wang D, Muller S, Fan S, Sun SY, , Gu TL, , Chen ZG, , Shin DM, Chen J. 2010. p90 ribosomal S6 kinase 2 promotes invasion and metastasis of human head and neck squamous cell carcinoma cells. *Journal of Clinical Investigation* **120**:1165–1177. DOI: <https://doi.org/10.1172/JCI40582>, PMID: 20234090
- Kanke T**, Macfarlane SR, Seatter MJ, Davenport E, Paul A, McKenzie RC, Plevin R. 2001. Proteinase-activated receptor-2-mediated activation of stress-activated protein kinases and inhibitory kappa B kinases in NCTC 2544 keratinocytes. *Journal of Biological Chemistry* **276**:31657–31666. DOI: <https://doi.org/10.1074/jbc.M100377200>, PMID: 11413129
- Kanther M**, Sun X, Mühlbauer M, Mackey LC, Flynn EJ, Bagnat M, Jobin C, Rawls JF. 2011. Microbial colonization induces dynamic temporal and spatial patterns of NF- κ B activation in the zebrafish digestive tract. *Gastroenterology* **141**:197–207. DOI: <https://doi.org/10.1053/j.gastro.2011.03.042>, PMID: 21439961
- Kawaguchi M**, Takeda N, Hoshiko S, Yorita K, Baba T, Sawaguchi A, Nezu Y, Yoshikawa T, Fukushima T, Kataoka H. 2011. Membrane-bound serine protease inhibitor HAI-1 is required for maintenance of intestinal epithelial

- integrity. *The American Journal of Pathology* **179**:1815–1826. DOI: <https://doi.org/10.1016/j.ajpath.2011.06.038>, PMID: 21840293
- Kimmel CB**, Ballard WW, Kimmel SR, Ullmann B, Schilling TF. 1995. Stages of embryonic development of the zebrafish. *Developmental Dynamics* **203**:253–310. DOI: <https://doi.org/10.1002/aja.1002030302>, PMID: 8589427
- Lee RT**, Asharani PV, Carney TJ. 2014. Basal keratinocytes contribute to all strata of the adult zebrafish epidermis. *PLOS ONE* **9**:e84858. DOI: <https://doi.org/10.1371/journal.pone.0084858>, PMID: 24400120
- Lin Q**, Low LWL, Lau A, Chua EWL, Matsuoka Y, Lian Y, Monteiro A, Tate S, Gunaratne J, Carney TJ. 2019. Tracking genome-editing and associated molecular perturbations by SWATH mass spectrometry. *Scientific Reports* **9**:15240. DOI: <https://doi.org/10.1038/s41598-019-51612-z>, PMID: 31645615
- List K**, Szabo R, Molinolo A, Sriuranpong V, Redeye V, Murdock T, Burke B, Nielsen BS, Gutkind JS, Bugge TH. 2005. Deregulated matriptase causes ras-independent multistage carcinogenesis and promotes ras-mediated malignant transformation. *Genes & Development* **19**:1934–1950. DOI: <https://doi.org/10.1101/gad.1300705>, PMID: 16103220
- Macfarlane SR**, Sloss CM, Cameron P, Kanke T, McKenzie RC, Plevin R. 2005. The role of intracellular Ca²⁺ in the regulation of proteinase-activated receptor-2 mediated nuclear factor kappa B signalling in keratinocytes. *British Journal of Pharmacology* **145**:535–544. DOI: <https://doi.org/10.1038/sj.bjp.0706204>, PMID: 15821758
- Maeda H**, Fukuyasu Y, Yoshida S, Fukuda M, Saeki K, Matsuno H, Yamauchi Y, Yoshida K, Hirata K, Miyamoto K. 2004. Fluorescent probes for hydrogen peroxide based on a non-oxidative mechanism. *Angewandte Chemie International Edition* **43**:2389–2391. DOI: <https://doi.org/10.1002/anie.200452381>, PMID: 15114569
- Martin CE**, List K. 2019. Cell surface-anchored serine proteases in Cancer progression and metastasis. *Cancer and Metastasis Reviews* **38**:357–387. DOI: <https://doi.org/10.1007/s10555-019-09811-7>, PMID: 31529338
- Mathias JR**, Dodd ME, Walters KB, Rhodes J, Kanki JP, Look AT, Huttenlocher A. 2007. Live imaging of chronic inflammation caused by mutation of zebrafish Hai1. *Journal of Cell Science* **120**:3372–3383. DOI: <https://doi.org/10.1242/jcs.009159>, PMID: 17881499
- McCoy KL**, Traynelis SF, Hepler JR. 2010. PAR1 and PAR2 couple to overlapping and distinct sets of G proteins and linked signaling pathways to differentially regulate cell physiology. *Molecular Pharmacology* **77**:1005–1015. DOI: <https://doi.org/10.1124/mol.109.062018>, PMID: 20215560
- Méant A**, Gao B, Lavoie G, Nourredine S, Jung F, Aubert L, Tcherkezian J, Gingras AC, Roux PP. 2020. Proteomic analysis reveals a role for RSK in p120-catenin phosphorylation and melanoma Cell-Cell adhesion. *Molecular & Cellular Proteomics* **19**:50–64. DOI: <https://doi.org/10.1074/mcp.RA119.001811>, PMID: 31678930
- Morris DR**, Ding Y, Ricks TK, Gullapalli A, Wolfe BL, Trejo J. 2006. Protease-Activated Receptor-2 is essential for factor VIIa and Xa-Induced Signaling, Migration, and Invasion of Breast Cancer Cells. *Cancer Research* **66**:307–314. DOI: <https://doi.org/10.1158/0008-5472.CAN-05-1735>
- Nagaïke K**, Kawaguchi M, Takeda N, Fukushima T, Sawaguchi A, Kohama K, Setoyama M, Kataoka H. 2008. Defect of hepatocyte growth factor activator inhibitor type 1/serine protease inhibitor, Kunitz type 1 (Hai-1/Spint1) leads to ichthyosis-like condition and abnormal hair development in mice. *The American Journal of Pathology* **173**:1464–1475. DOI: <https://doi.org/10.2353/ajpath.2008.071142>, PMID: 18832587
- Niethammer P**, Grabher C, Look AT, Mitchison TJ. 2009. A tissue-scale gradient of hydrogen peroxide mediates rapid wound detection in zebrafish. *Nature* **459**:996–999. DOI: <https://doi.org/10.1038/nature08119>, PMID: 19494811
- Rattenholl A**, Seeliger S, Buddenkotte J, Schön M, Schön MP, Ständer S, Vergnolle N, Steinhoff M. 2007. Proteinase-activated receptor-2 (PAR2): a tumor suppressor in skin carcinogenesis. *Journal of Investigative Dermatology* **127**:2245–2252. DOI: <https://doi.org/10.1038/sj.jid.5700847>, PMID: 17476297
- Razzell W**, Evans IR, Martin P, Wood W. 2013. Calcium flashes orchestrate the wound inflammatory response through DUOX activation and hydrogen peroxide release. *Current Biology* **23**:424–429. DOI: <https://doi.org/10.1016/j.cub.2013.01.058>, PMID: 23394834
- Redd MJ**, Kelly G, Dunn G, Way M, Martin P. 2006. Imaging macrophage chemotaxis in vivo: studies of microtubule function in zebrafish wound inflammation. *Cell Motility and the Cytoskeleton* **63**:415–422. DOI: <https://doi.org/10.1002/cm.20133>, PMID: 16671106
- Renshaw SA**, Loynes CA, Trushell DM, Elworthy S, Ingham PW, Whyte MK. 2006. A transgenic zebrafish model of neutrophilic inflammation. *Blood* **108**:3976–3978. DOI: <https://doi.org/10.1182/blood-2006-05-024075>, PMID: 16926288
- Rigutto S**, Hoste C, Grasberger H, Milenkovic M, Communi D, Dumont JE, Corvilain B, Miot F, De D. 2009. Activation of dual oxidases Duox1 and Duox2: differential regulation mediated by camp-dependent protein kinase and protein kinase C-dependent phosphorylation. *The Journal of Biological Chemistry* **284**:6725–6734. DOI: <https://doi.org/10.1074/jbc.M806893200>, PMID: 19144650
- Romeo Y**, Zhang X, Roux PP. 2012. Regulation and function of the RSK family of protein kinases. *Biochemical Journal* **441**:553–569. DOI: <https://doi.org/10.1042/BJ20110289>, PMID: 22187936
- Rothwarf DM**, Zandi E, Natoli G, Karin M. 1998. IKK-gamma is an essential regulatory subunit of the I-kappaB kinase complex. *Nature* **395**:297–300. DOI: <https://doi.org/10.1038/26261>, PMID: 9751060
- Sales KU**, Friis S, Konkel JE, Godiksen S, Hatakeyama M, Hansen KK, Rogatto SR, Szabo R, Vogel LK, Chen W, Gutkind JS, Bugge TH. 2015. Non-hematopoietic PAR-2 is essential for matriptase-driven pre-malignant progression and potentiation of ras-mediated squamous cell carcinogenesis. *Oncogene* **34**:346–356. DOI: <https://doi.org/10.1038/onc.2013.563>, PMID: 24469043
- Salhi A**, Farhadian JA, Giles KM, Vega-Saenz de Miera E, Silva IP, Bourque C, Yeh K, Chhangawala S, Wang J, Yeh F, Zhang DY, Hernando-Monge E, Houvras Y, Osman I. 2015. RSK1 activation promotes invasion in nodular

- melanoma. *The American Journal of Pathology* **185**:704–716. DOI: <https://doi.org/10.1016/j.ajpath.2014.11.021>, PMID: 25579842
- Sapkota GP**, Cummings L, Newell FS, Armstrong C, Bain J, Frodin M, Grauert M, Hoffmann M, Schnapp G, Steegmaier M, Cohen P, Alessi DR. 2007. BI-D1870 is a specific inhibitor of the p90 RSK (ribosomal S6 kinase) isoforms in vitro and in vivo. *Biochemical Journal* **401**:29–38. DOI: <https://doi.org/10.1042/BJ20061088>, PMID: 17040210
- Schäfer M**, Werner S. 2008. Cancer as an overhealing wound: an old hypothesis revisited. *Nature Reviews Molecular Cell Biology* **9**:628–638. DOI: <https://doi.org/10.1038/nrm2455>, PMID: 18628784
- Schechter NM**, Brass LF, Lavker RM, Jensen PJ. 1998. Reaction of mast cell proteases tryptase and chymase with protease activated receptors (PARs) on keratinocytes and fibroblasts. *Journal of Cellular Physiology* **176**:365–373. DOI: [https://doi.org/10.1002/\(SICI\)1097-4652\(199808\)176:2<365::AID-JCP15>3.0.CO;2-2](https://doi.org/10.1002/(SICI)1097-4652(199808)176:2<365::AID-JCP15>3.0.CO;2-2), PMID: 9648924
- Schepis A**, Barker A, Srinivasan Y, Balouch E, Zheng Y, Lam I, Clay H, Hsiao CD, Coughlin SR. 2018. Protease signaling regulates apical cell extrusion, cell contacts, and proliferation in epithelia. *Journal of Cell Biology* **217**:1097–1112. DOI: <https://doi.org/10.1083/jcb.201709118>, PMID: 29301867
- Schreck R**, Rieber P, Baeuerle PA. 1991. Reactive oxygen intermediates as apparently widely used messengers in the activation of the NF-kappa B transcription factor and HIV-1. *The EMBO Journal* **10**:2247–2258. DOI: <https://doi.org/10.1002/j.1460-2075.1991.tb07761.x>, PMID: 2065663
- Sheng J**, Deng X, Zhang Q, Liu H, Wang N, Liu Z, Dai E, Deng Q. 2019. PAR-2 promotes invasion and migration of esophageal Cancer cells by activating MEK/ERK and PI3K/Akt signaling pathway. *International Journal of Clinical and Experimental Pathology* **12**:787–797. PMID: 31933886
- Shi K**, Queiroz KC, Stap J, Richel DJ, Spek CA. 2013. Protease-activated receptor-2 induces migration of pancreatic Cancer cells in an extracellular ATP-dependent manner. *Journal of Thrombosis and Haemostasis* **11**:1892–1902. DOI: <https://doi.org/10.1111/jth.12361>, PMID: 23899344
- Shi GX**, Yang WS, Jin L, Matter ML, Ramos JW. 2018. RSK2 drives cell motility by serine phosphorylation of LARG and activation of rho GTPases. *PNAS* **115**:E190–E199. DOI: <https://doi.org/10.1073/pnas.1708584115>, PMID: 29279389
- Sivak JM**, Petersen LF, Amaya E. 2005. FGF signal interpretation is directed by sprouty and spread proteins during mesoderm formation. *Developmental Cell* **8**:689–701. DOI: <https://doi.org/10.1016/j.devcel.2005.02.011>, PMID: 15866160
- Sulzmaier FJ**, Young-Robbins S, Jiang P, Geerts D, Precht AM, Matter ML, Kesari S, Ramos JW. 2016. RSK2 activity mediates glioblastoma invasiveness and is a potential target for new therapeutics. *Oncotarget* **7**:79869–79884. DOI: <https://doi.org/10.18632/oncotarget.13084>
- Szabo R**, Molinolo A, List K, Bugge TH. 2007. Matriptase inhibition by hepatocyte growth factor activator inhibitor-1 is essential for placental development. *Oncogene* **26**:1546–1556. DOI: <https://doi.org/10.1038/sj.onc.1209966>, PMID: 16983341
- Szabo R**, Rasmussen AL, Moyer AB, Kosa P, Schafer JM, Molinolo AA, Gutkind JS, Bugge TH. 2011. c-Met-induced epithelial carcinogenesis is initiated by the serine protease matriptase. *Oncogene* **30**:2003–2016. DOI: <https://doi.org/10.1038/onc.2010.586>, PMID: 21217780
- Tanaka Y**, Sekiguchi F, Hong H, Kawabata A. 2008. PAR2 triggers IL-8 release via MEK/ERK and PI3-kinase/Akt pathways in GI epithelial cells. *Biochemical and Biophysical Research Communications* **377**:622–626. DOI: <https://doi.org/10.1016/j.bbrc.2008.10.018>, PMID: 18854173
- Tanimura S**, Takeda K. 2017. ERK signalling as a regulator of cell motility. *The Journal of Biochemistry* **162**:145–154. DOI: <https://doi.org/10.1093/jb/mvx048>, PMID: 28903547
- Thisse C**, Thisse B. 2008. High-resolution in situ hybridization to whole-mount zebrafish embryos. *Nature Protocols* **3**:59–69. DOI: <https://doi.org/10.1038/nprot.2007.514>, PMID: 18193022
- Turvey SE**, Durandy A, Fischer A, Fung SY, Geha RS, Gewies A, Giese T, Greil J, Keller B, McKinnon ML, Neven B, Rozmus J, Ruland J, Snow AL, Stepensky P, Warnatz K. 2014. The CARD11-BCL10-MALT1 (CBM) signalosome complex: stepping into the limelight of human primary immunodeficiency. *Journal of Allergy and Clinical Immunology* **134**:276–284. DOI: <https://doi.org/10.1016/j.jaci.2014.06.015>, PMID: 25087226
- van der Merwe JQ**, Moreau F, MacNaughton WK. 2009. Protease-activated receptor-2 stimulates intestinal epithelial chloride transport through activation of PLC and selective PKC isoforms. *American Journal of Physiology-Gastrointestinal and Liver Physiology* **296**:G1258–G1266. DOI: <https://doi.org/10.1152/ajpgi.90425.2008>, PMID: 19359428
- van Eeden FJ**, Granato M, Schach U, Brand M, Furutani-Seiki M, Haffter P, Hammerschmidt M, Heisenberg CP, Jiang YJ, Kane DA, Kelsh RN, Mullins MC, Odenthal J, Warga RM, Nüsslein-Volhard C. 1996. Genetic analysis of fin formation in the zebrafish, *Danio rerio*. *Development* **123**:255–262. DOI: <https://doi.org/10.1242/dev.123.1.255>, PMID: 9007245
- Wang P**, DeFea KA. 2006. Protease-activated receptor-2 simultaneously directs beta-arrestin-1-dependent inhibition and Galphaq-dependent activation of phosphatidylinositol 3-kinase. *Biochemistry* **45**:9374–9385. DOI: <https://doi.org/10.1021/bi0602617>, PMID: 16878972
- Zhao P**, Metcalf M, Bunnett NW. 2014. Biased signaling of Protease-Activated receptors. *Frontiers in Endocrinology* **5**:67. DOI: <https://doi.org/10.3389/fendo.2014.00067>